High-Resolution Ultraviolet Spectroscopy of Neutral and Ionic Clusters: Hydrogen Bonding and the External Heavy Atom Effect

Hans Jürgen Neusser* and Klaus Siglow

Institut für Physikalische und Theoretische Chemie, Technische Universität München, Lichtenbergstrasse 4, D-85748 Garching, Germany

Received January 12, 2000

Contents

I. Introduction

High-resolution spectroscopy has provided detailed information about the structure and dynamics of many different molecules. During the past decade its range of application has been extended from chemically bound to weakly bound van der Waals molecules. Because of their instability, the small binding energies of van der Waals clusters, and their difficult production, a series of problems emerged which showed that obtaining high-resolution spectra of clusters was a more challenging task than that of stable chemically bound molecules. This work reviews some of the ways in which these problems have been addressed and describes the results obtained for a number of weakly bound complexes.

The goal of cluster investigations is to obtain a microscopic understanding of the van der Waals bonding or the hydrogen bonding or of charge-induced interaction mechanisms. This goal necessitates the investigation of the structure and intermolecular dynamics of the weakly bound complexes, i.e., the vibrational dynamics within the intermolecular potential. Therefore, it is highly desirable to achieve an as-high-as-possible spectral resolution leading to the selective excitation and observation of individual quantum states. The conventional techniques providing quantum-state resolution are microwave spectroscopy and infrared spectroscopy. Indeed, these techniques have provided a lot of valuable information on clusters. However, microwave spectroscopy is limited to the investigation of ground-state levels and high-resolution infrared spectroscopy has hitherto been limited to clusters of small molecules. In the case of microwave spectroscopy, it is difficult to find the absorption lines of a van der Waals complex when the structure is not known. Additionally, special slit nozzles have to be used to detect the absorption of the infrared photon by a direct absorption measurement which up to now has limited its application to clusters of small molecules. High-resolution rotationally resolved ultraviolet (UV) laser spectroscopy often can provide the information necessary for structure determination. Several UV techniques have been developed to provide the necessary spectral resolution, the particle selectivity, etc., to detect clusters within the cold molecular beam where they are produced.

This article reports on new developments and results of high-resolution UV spectroscopy since 1994. The early progress in rotationally resolved UV spectroscopy of van der Waals clusters has been described in several review articles.[1] This article highlights the developments since then. Application of high-resolution UV spectroscopy has been extended from van der Waals bonding to hydrogen bonding in aromatic-molecule•water clusters. New methods based on the detection of Rydberg states were developed to achieve rotational resolution in ionic aromatic-molecule•noble-

* To whom correspondence should be addressed. Fax: ++49 89 28913412. E-mail: neusser@ch.tum.de.

10.1021/cr9900578 CCC: $35.00
Published on Web 10/04/2000

Hans Jürgen Neusser was born in 1943 in Troppau. He studied physics at the Technische Universität München, where he received his Dr.rer.nat. degree with Professor W. Kaiser on laser-produced plasmas. Subsequently he was working with Professor E. W. Schlag and gained his Habilitation degree in physical chemistry in 1977 for work on two-photon spectroscopy of molecules. In 1978 he was appointed Privatdozent and 1979 Professor of Physical Chemistry at the Technische Universität München. In 1983 he received the Chemie-Preis of the Akademie der Wissenschaften zu Göttingen for his work in the field of two-photon spectroscopy, multiphoton ionization, and Doppler-free high-resolution molecular spectroscopy. He was a visiting fellow of the JSPS in Japan and received the Willstätter Lecture of the Deutsche Chemische Gesellschaft. He has authored and co-authored more than 160 scientific papers and a monograph. At present his main interests focus on laser spectroscopy of highly excited electronic states in molecules and clusters and on ultrafast dynamic and charge-transfer processes in isolated molecules.

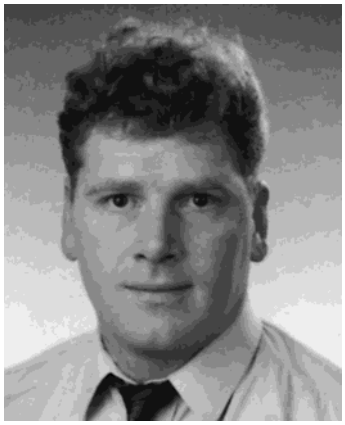

Klaus Siglow was born in München, Germany, in 1968. He received his Diploma in Physics in 1996 from the Technische Universität München. Since 1995, he has been working in the research group of Hans Jürgen Neusser at the Institut für Physikalische und Theoretische Chemie of the Technische Universität München. His research interests include the spectroscopy of highly excited electronic states in polyatomic molecules and weakly bound clusters thereof. His doctoral research—graduation in August 2000—includes the investigation of resolved high Rydberg states in benzene and benzene·rare-gas clusters and the application of the spectroscopy of high Rydberg states to high-resolution studies of the cationic states including effects of enhanced spin–orbit coupling and the dissociation dynamics of these cationic systems.

gas complexes. The selective excitation of high Rydberg states ($50 \lesssim n \lesssim 100$) and their computer-assisted extrapolation allows one to determine the series limits representing the rotational levels in various vibrational bands of the cluster. We present results for the prototype benzene·noble-gas dimers leading to resolution of individual rotational levels in their cationic states to illustrate the method.

II. Neutral Clusters

A. Methods

1. Mass-Selective Techniques

Up to now nearly all high-resolution UV experiments have been performed on neutral clusters as they are directly produced in the adiabatic expansion of the molecular beam. However, the problem arises that not only a specific cluster size is produced, but a mixture of clusters of different composition of the molecules is present in the supersonic expansion. For this reason a mass selective method for detection of cluster spectra is advantageous. This can be realized for UV spectroscopy if double-resonance techniques such as resonance-enhanced two-photon ionization (REMPI) are used. Here, the spectrum of the intermediate state excited by the absorption of one photon is measured by monitoring the ion current after mass selection, e.g., in a time-of-flight mass spectrometer.[2] This technique has been successfully applied to measure vibrationally resolved UV spectra of many molecules and clusters. To achieve rotational resolution, additional refinements are necessary; the Doppler width has to be reduced, e.g., by the use of a skimmer selecting the central part of the molecular beam, thus reducing the transverse velocity component, and a pulsed nanosecond laser source with a frequency width as narrow as possible is necessary to combine high resolution with high intensity.

Figure 1 shows the experimental setup for high-resolution spectroscopy of neutral clusters.[3,4] Typically, for the production of molecule·water clusters, a few bar backing pressure of Ar and 10 mbar of water are expanded through a specially developed heated reservoir of the fluid aromatic molecule just in front of a pulsed valve with 200 μm orifice into the first vacuum chamber. The gas throughput is limited by the short pulse opening of the valve, which proceeds synchronously with the arrival of the laser light pulses. Through the cooling in the expansion, various homo- and heteroclusters of the aromatic molecule, the noble gas, and water are formed. A conical-shaped skimmer peels away the outer shell of the molecular beam, enabling the expansion of the central part into a second vacuum chamber with a lower background pressure where the interaction with the light occurs. Thereby, the Doppler broadening amounts to about 0.05 cm^{-1} in a bulk gas of medium sized (100 amu) molecules and is reduced to some 40 MHz or 0.001 cm^{-1}. The narrowband light of a cw-single-mode ring dye laser is pulse-amplified to a peak power of 1 MW in a three-stage excimer-laser-pumped amplifier setup. The generated visible light pulses of 15 ns are Fourier transform-limited with a frequency width of less than 40 MHz, yielding a spectral resolution of about 70 MHz. The high peak power of 1 MW allows efficient frequency doubling of the visible light into the ultraviolet spectral region, needed for the excitation of the $S_1 \leftarrow S_0$ transition in the aromatic-molecule·water clusters through the absorption of one photon. The subsequent absorption of a UV photon stemming from a relatively broad

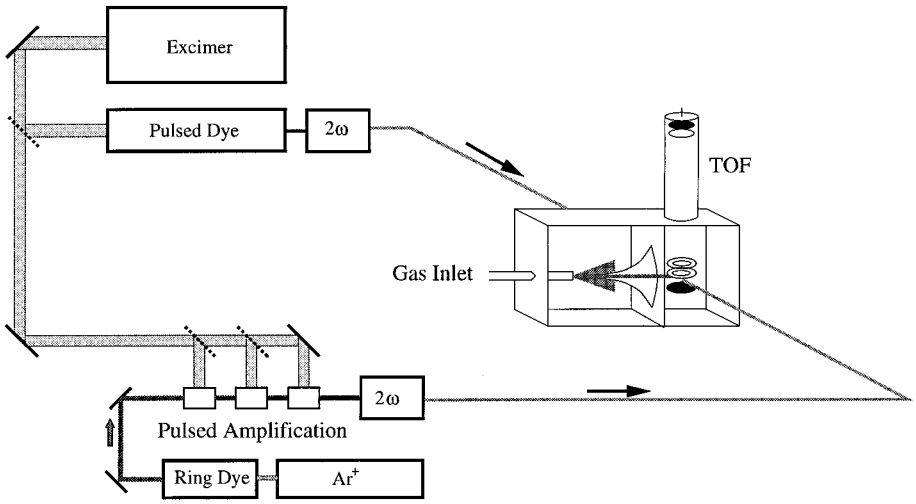

Figure 1. Experimental setup for the recording of high-resolution UV spectra of clusters of aromatic molecules with water by mass-selected resonance-enhanced two-photon ionization. A high spectral resolution of 70 MHz is obtained by pulsed amplification of a single-mode continuous wave dye laser and subsequent frequency doubling. The clusters are produced in a cold supersonic beam, and a skimmer is used for reduction of the Doppler broadening.

band dye laser, simultaneously pumped by the excimer laser, brings the excited (to the S_1 state) complexes into the ionization continuum. The ions are mass-selected and detected in a simple home-built time-of-flight mass spectrometer with mass resolution of about 200. Thus, the spectra of different clusters can be measured simultaneously by integrating the mass peaks with gated integrators. Simultaneously recorded are the calibration signals with fractions of the visible cw laser light. The relative frequency calibration signal is provided by a 150 MHz Fabry−Perot interferometer transmission spectrum and the absolute frequency calibration signal by a calibrated iodine vapor fluorescence excitation spectrum.[5]

2. Other Methods

Though most of the experiments on clusters discussed in this work have been performed with mass-selective techniques, we would like to briefly discuss other promising methods used for rotationally resolved UV spectroscopy of clusters. It is also possible to monitor the fluorescence after absorption of a UV photon. In this case, no mass selection is available but cw single-mode lasers can be used yielding a high spectral resolution down to 1 MHz in the best case. Several cluster spectra measured with this technique are discussed below.

To complete this brief summary of methods of rotationally resolved spectroscopy of clusters, a coherent technique operating in the time domain is addressed. In rotation coherence spectroscopy, a coherent ensemble of rotating molecules is excited by picosecond or femtosecond laser pulses and the rephasing of the macroscopic polarization is detected.[6,7] From a measurement of the recurrence time, rotational constants were obtained for aromatic-molecule·rare-gas clusters and dimers of aromatic molecules. Experiments have been performed in different laboratories.[8−13] The systems studied with this technique are discussed in a recent review by Felker and co-workers.[8]

3. Rotational Band Analysis

The rotational structure of vibronic bands in clusters is more complicated and congested than in molecules. This is due to the larger mass of the cluster, its lower symmetry, and the additional internal degrees of freedom. This makes the interpretation of the rotational structure more complicated; an assignment of the large number of rotational transitions is a lengthy procedure, and in many cases individual lines are no longer resolved so that even an assignment is impossible. For these reasons it is useful to apply pattern recognition methods for the simulation and interpretation of the complex spectra of clusters. This has become possible by the use of modern computers after the fast development of computational power and advanced algorithms. The details of the algorithm and the error handling of this procedure have been described elsewhere.[14] Here we would like to demonstrate the basic results.

The use of correlation methods for the simulation and interpretation of UV spectra was demonstrated by Levy and co-workers for spectra of organic molecules and clusters.[15,16] Other algorithms require an assignment of theoretical quantum numbers to experimental lines before their positions can be fit.[17−19] Recently, we presented another approach for fitting of unresolved or overlapping lines without a preceding assignment. This is the correlation automated rotational fitting (CARF) algorithm[20] which makes a direct fit of the experimental data possible without any preceding assignment of the lines.

In the CARF procedure, the experimental spectrum is cross correlated with different calculated spectra and the maximum of the so-obtained cross correlation is a criterion for the quality of the simulation. The calculation includes a simulation of the spectrum and convolution of the simulated stick spectrum with a Gaussian line shape function. The cross correlation can be taken as a value for area overlap between theoretical and experimental spectra as a function of their relative position. To reduce the computational time, fast Fourier transform (FFT) methods for

calculation of the cross correlation according to the correlation theorem are useful.[21]

More than 10 000 different simulations have to be automatically generated and compared with the experimental spectra. In a first step, the offset between the simulated and calculated spectrum is determined by the positioning of the cross correlation maximum. In a second step, the amplitude of the correlation maximum is used as a criterion for the quality of the rotational constants.

By changing the rotational constants either by hand and visual inspection or by fitting algorithms, such as downhill simplex, direction set (Powells's), conjugate gradient, or simulated annealing,[21] the rotational constants are improved step by step to finally yield a theoretical spectrum. Since the rotational contour depends not only on the rotational constants but also on other parameters, such as the rotational temperature, line shape, line width, and statistical weights, and on nonlinearities such as saturation, extreme care has to be taken to start the fit with reasonable values of these constants. Every fitting algorithm has its special advantages, e.g., different convergence radii and step adaptation. For this reason, one must carefully choose the fitting algorithm in order to obtain fast convergence and avoid false maxima.

The resulting correlation function of the experimental and calculated spectra for different rotational constants is a peak with multidimensional Gaussian shape whose absolute height is used as a criterion for the quality of the simulated spectrum. In practice, the different fitting procedures described above can only handle a limited number of adjustable parameters. Therefore, the analysis of complicated spectra is performed in several steps. A preceding autocorrelation of the measured spetrum indicates possible torsional splittings and rotational subbands. Following the results of the autocorrelation analysis, a suitable model Hamiltonian for the simulation of the measured spectra is selected. Subbands or torsional splittings can be included to evaluate the simulated spectrum, thus increasing the number of parameters to be fit to the experimental spectrum. Making reasonable assumptions will then help to iteratively fit groups of parameters to the experimental spectrum.

As an example. for the quality of the applied technique, the maximum of the correlation of the experimental and theoretical spectrum of the $S_1 \leftarrow S_0$ transition of phenol·water is plotted as a function of the excited-state rotational constants A' and B' in Figure 2. This plot represents a projection of the multidimensional Gaussian shape on the two coordinates. The appearance of a single peak demonstrates that the value for each constant is unambiguous. The height of the peak and its slope as well as the small numbers of side maxima promise fast convergence within the convergence radius. Note that the cross correlation peak in Figure 2 has only one maximum. This not only demonstrates the usefulness of the algorithm, but also gives a single value for the rotational constants. The quality of the determined rotational constants is demonstrated in Figure 11 of section II.C, where the experimental and theoretical spectra are compared to each other. This is also an example where a torsional splitting leading to independent sets of rotational constants are successfully handled by the CARF method.

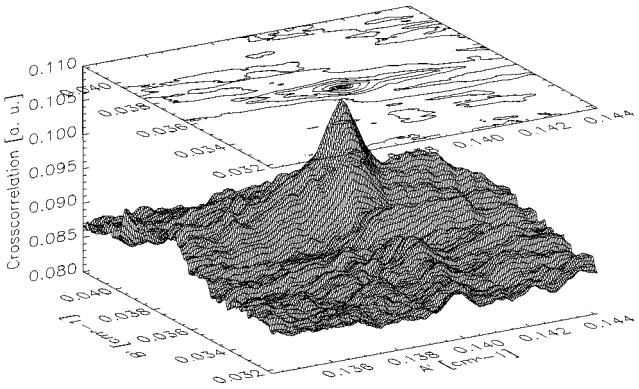

Figure 2. Two-dimensional maximum of the cross correlation between the experimental and a theoretical $S_1 \leftarrow S_0$ origin spectrum of phenol·water (see Figure 11) as a function of the rotational constants A' and B'. The contour lines represent positions with equal correlation. The strong central peak yields the rotational constants for the best fit of the experimental spectrum. For explanation, see text. (Reprinted with permission from ref 14. Copyright 1998 American Institute of Physics.)

B. Structure Information

First, the technique of mass-resolved high resolution was applied to prototype cluster systems, such as benzene·Ar and benzene·Ar_2.[17,22] Meanwhile, a variety of aromatic·noble-gas clusters has been investigated with this technique and fluorescence detection high-resolution UV spectroscopy.[3,4] Among these clusters are benzonitrile·Ar[20] and indole·Ar.[23] These results are not discussed in this review as we would like to focus attention on dimers of these molecules with water. The main goal of these investigations is to find information on the character of the hydrogen bonding for different chemical surroundings provided by the various aromatic systems. In this section we discuss two selected aromatic-molecule·water systems forming two different types of hydrogen or hydrogen-like bonding.

1. Benzonitrile·Water

Benzonitrile is a molecule of much current interest. The reasons for this interest are 2-fold. Benzonitrile and its amino derivatives are basic molecules for the study of internal charge-transfer processes leading to a structural change and, in particular in the latter case, to a twisting of the molecule after excitation.[24,25] The charge-transfer process is expected to be influenced by the solvent. An experimental indication of the twisting process is the appearance of a red-shifted fluorescence when the benzonitrile molecules were dissolved in polar solvents. Further, benzonitrile·water represents a prototype system of water weakly bound to a cyano group by hydrogen bonding. Because of the large dipole moment of benzonitrile (4.18 D[26]), an influence of the dipole−dipole interaction on the hydrogen bonding might be expected. The character of the bonding may differ from the hydrogen

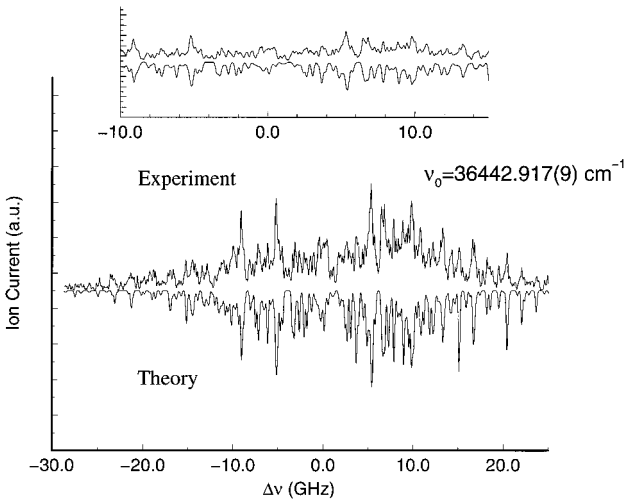

Figure 3. Highly resolved UV spectrum of the $S_1 \leftarrow S_0$, 0_0^0 transition of the benzonitrile·water complex. Upright traces: experimental spectrum. Inverted traces: calculated spectrum using the rotational constants found by correlation automated rotational fitting (CARF). Top: central part of the spectrum on a magnified scale. $\nu_0 = 36\ 422.917(9)$ cm^{-1} is the frequency of the band origin. (Reprinted with permission from ref 31. Copyright 1997 Verlag der Feitschrift für Naturforschung.)

bonding in other aromatic molecules such as phenol·water,[18] pyridone·water,[27] and indole·water.[28−30]

The experimental setup used in the high-resolution UV experiments[31] was described above. Ar at a backing pressure of 5 bar and 10 mbar of water was expanded through a heated (60 °C) reservoir of fluid benzonitrile located in front of a pulsed valve with a 200 μm orifice. The laser system providing the Fourier transform limited light pulses was operated with Rhodamine 110, while Coumarin 307 dye was used for amplification. To avoid broadening of the rotational lines, the pulse energy was reduced to 0.2 mJ. This equals the pulse energy of the second ionizing laser pulse originating from a commercial broad band dye laser. The measured high-resolution spectrum is shown in Figure 3. The rotational structure is not of *c*-type but represents a mixed *a*- and *b*-type spectrum. From this result we can exclude a position of the water above the molecular plane (which is observed for Ar in the benzonitrile·Ar complex[20]); the water oxygen must be located near the benzonitrile plane. This result was the starting point for a microwave experiment by the Kiel microwave group. It provided starting values for the rotational constants for a guess of the scanning range. In the predicted frequency range the cluster lines could be identified in the microwave experiment and the rotational constants in the electronic ground state were determined with high precision (see Table 1). Using the set of ground-state rotational constants in a second step, we simulated the rotational structure of the UV spectrum to find a set of rotational constants for the electronically excited S_1 state. Since an assignment of single lines is not possible given the congested structure of the spectrum, we used the correlation automated rotational fitting (CARF) procedure described in section II.A. Best agreement was obtained for a rotational temperature of 1 K. The intensity ratio of *a*- to *b*-type transition was adjusted to 19:81 from the microwave results. The resulting theoretical spectrum is shown in the lower inverted trace of Figure 3.

Table 1. Experimental Rotational and Centrifugal Distortion Constants and Moments of Inertia I_g of the Benzonitrile·Water Complex[a]

benzonitrile−H_2O	$H_2{}^{16}O$ (S_0)	$H_2{}^{18}O$ (S_0)	$H_2{}^{16}O$ (S_1)
A/MHz	2882.2886(22)	2825.0638(44)	2822(1)
B/MHz	995.71865(39)	957.02927(41)	984(1)
C/MHz	740.49971(23)	715.26447(24)	729(1)
κ	−0.7617	−0.7706	−0.7560
D'_J/kHz	0.2576(15)	0.2598(25)	
D'_{JK}/kHz	−0.678(16)	−0.763(57)	
D'_K/kHz	4.21(45)	4.54(80)	
I_a/amu Å^2	175.338	178.890	179.109
I_b/amu Å^2	507.549	528.068	513.436
I_c/amu Å^2	682.480	706.559	693.251
origin/cm^{-1}			36442.923(9)

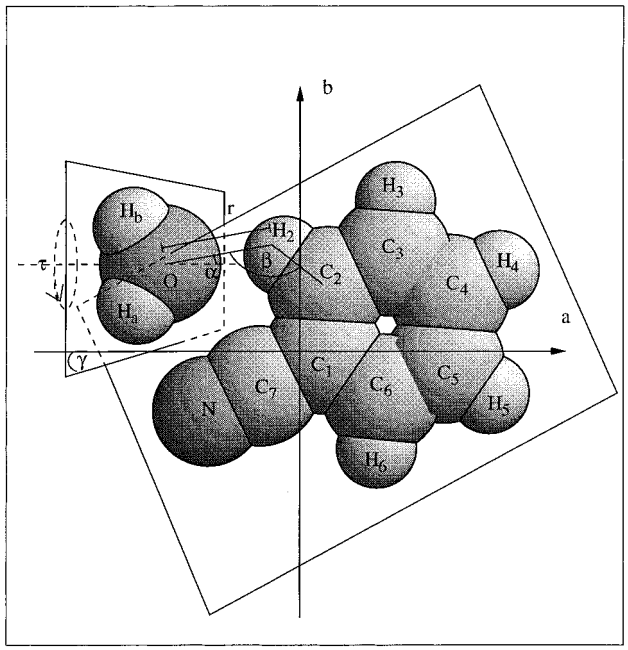

Figure 4. Experimental structure of the benzonitrile·water complex. For numbering and geometric parameters, see text. Only the structure with the torsion angle $\tau = 0$ is shown. γ describes the inclination of the water plane with respect to the benzonitrile plane. (Reprinted with permission from ref 31. Copyright 1997 Verlag der Feitschrift für Naturforschung.)

The experimental structure of the benzonitrile·water complex is shown in Figure 4. It was determined from the measured rotational constants under the assumption that the structures of benzonitrile[32,33] and water[34] do not change with complexation. This appears to be reasonable if one is mainly interested in the intermolecular structure parameters (see also below, section II.B.2). Furthermore, we think that internal structure changes are expected to be smaller than, e.g., in phenol·water[18] and pyridone·water,[27] since the intermolecular bond length is longer in benzonitrile·water. There are some uncertainties concerning the exact position of the hydrogen atoms. Recent microwave experiments with deuterated water point to an out-of-plane position of the water hydrogens with the center of mass of the water molecule within the plane of benzonitrile.[35] The water

Table 2. Structural Parameters of the Benzonitrile·Water Cluster in the S_0 and S_1 State Obtained with a r_0 fit

			with/without diffuse functions	
	S_0 (MW)	S_1 (UV)	S_0 (HF)	S_1 (CIS)
r [Å]	2.477(4)	2.457(2)	2.493/2.573	2.479/2.550
β	143.34(2)°	141.91(3)°	148.9°/147.4°	149.3°/148.1°
γ	33.7(60)°	0°		
r_{CM}[Å]	4.152(3)	4.155	4.240/4.371	4.237/4.404
r_{HN} [Å]	2.612(16)	2.631	2.634/2.502	2.659/2.509

[a] r: distance of the *ortho*-hydrogen atom in benzonitrile from the water oxygen atom. r_{CM}: distances of the centers of mass of the benzonitrile and the water molecules. r_{HN}: distance of the water hydrogen atom next to the nitrogen atom from the latter. For definition of β and γ, see text and Figure 4.

molecule is in a nested position between CN groups and the *ortho*-hydrogen. The results for the experimental structural parameters in the S_0 and S_1 state are given in Table 1.

The bond length of $r = 2.477(4)$ Å between the *ortho*-hydrogen of benzonitrile and the water oxygen is between the typical bond length of a van der Waals bonded (e.g., van der Waals bond length of benzonitrile·Ar in S_0 (S_1): 3.598 (3.52) Å[20]) and a hydrogen-bonded system (e.g., phenol·water; the distance from the phenol's hydrogen to the water's oxygen in S_0 (S_1) is roughly 1.97 (1.93) Å[18]). The two links of the water to the ortho hydrogen and the CN group should be compared to recent findings in pyridone·water.[27] In benzonitrile·water the distance of the water oxygen to the *ortho*-hydrogen in S_0 (S_1) is 2.477 (2.46) Å, whereas the distance r_{HN} between the water hydrogen and the benzonitrile nitrogen is 2.612 (2.63) Å. The respective distances in pyridone·water derived from the Kraitchman's equations are smaller and increase upon electronic excitation. The distance of the water oxygen to the nearest pyridone hydrogen is 2.01 (2.05) Å; the water hydrogen is 1.97 (2.05) Å apart from the pyridone oxygen.[27] This might be due to the different position of the water molecule in the two systems, with the nested character of the water position in benzonitrile·water and the side-on position in pyridone·water.

These results show that the bonding in the benzonitrile·water complex has hydrogen as well as van der Waals character. The experimental data also show that there are minor structure changes between S_0 and S_1 concerning the position of the water relative to the center of mass of the benzonitrile molecule (r_{CM} in Table 2). The change of the intermolecular bond length upon electronic excitation is larger than the distance change between the centers of mass of the two molecules. The changes can be explained by the structure change from S_0[32] to S_1[20] of the benzonitrile monomer. This means that the intermolecular bonding is only slightly affected by the electronic excitation. For comparison, the changes of the bond length upon electronic excitation in complexes between aromatics and rare gases are larger. For example, in benzene·Ar, the Ar is located above the ring at a distance of 3.58 (3.52) Å S_0 (S_1).[17] The larger change of the bond distance after electronic excitation is caused by the influence of the π-electron excitation in the benzene ring on the van der Waals bonding due to the increasing polarizability in the electronically excited benzene. The in-plane, side-on position of the water in benzonitrile·water is less influenced by the electronic $\pi-\pi^*$ excitation localized in the ring.

Since an experimental determination of the positions of the water hydrogen atoms in the benzonitrile·water complex is complicated,[35] we performed ab initio calculations of the structure of the benzonitrile monomer and its complex with water in the S_0 state at the HF level and for the excited S_1 state with the single-excitation configuration method (CIS).[36] The calculations were performed with the correlation-consistent cc-pVDZ basis set (for brief discussion of the level and basis set combination used, see section II.B.2). We calculated the structures without using diffuse functions, with diffuse functions (taken from 6-31+G) at heavy atoms (cc-pVDZ+), and with diffuse functions (taken from 6-31++G) for all atoms (cc-pVDZ++). The geometries of the clusters were fully optimized, and the resulting structure parameters are listed in Table 2. The computed oxygen position in the cluster agrees quite well with the experiment (see Figure 4). The oxygen is attached to one of the *ortho*-hydrogens of benzonitrile in a van der Waals type binding. However, the positions of the two water hydrogen atoms differ from the experimental structure[31,35] when calculating the cluster geometry without diffuse function. These calculated structures (in S_0 and S_1) show an asymmetric position of the two water hydrogens with respect to the plane of benzonitrile and which are shifted toward the nitrogen atom in benzonitrile. Thus, between the lone electron pair of the nitrogen and the closest water hydrogen atom there is a bond with hydrogen bonding character and a bond angle $\angle(OH_{H_2O}N)$ of 130.1° in the S_0 and 125.7° in the S_1 state. Most likely the other water hydrogen is also bonded to the nitrogen atom, but the bonding is very weak because this hydrogen atom is farther away from the nitrogen by 0.7 Å. The computed structures including diffuse functions yield the experimentally concluded in-plane position of the water molecule. Differences of bond lengths calculated from the cc-pVDZ+ and the ccpVDZ++ type basis sets are within 1 mÅ.

From experiment, we find that on electronic excitation from S_0 to S_1 the bond lengths increase on average by about 30 mÅ in the benzonitrile ring.[31] Theoretical and experimental data for the ground-state S_0 show minor alterations of the benzonitrile structure after complexation[31,32] (bond length changes $\lesssim$ 5 mÅ, bond angle changes $\lesssim$ 0.5°). The calculations also show that the structural changes on complexation are about the same when the benzonitrile molecule is excited to the S_1 state. This means that the structural changes of benzonitrile undergoing an electronic excitation from S_0 to S_1 are not influenced by clustering with the water molecule. However, because of the enlargement of the benzonitrile structure after electronic excitation, the water molecule seems to come closer to the chromophore. In fact, the changes of the distance of the centers of mass of benzonitrile and water are smaller ($\approx$1 mÅ) than the changes of the intermolecular distances ($\approx$10 mÅ) by

about 1 order of magnitude. We could find a shortening of the $r(O-H_{BzN})$ distance by 14 mÅ but, on the other hand, a lengthening of the $(H_{H_2O}-N)$ distance r_{HN} by 25 mÅ. This is mainly a consequence of the enlargement of the benzonitrile molecule after electronic excitation in agreement with the conclusions from experiment.

We convoluted the calculated stick spectrum in the lower inverted trace of Figure 3 with a Gaussian line shape of 180 MHz (fwhm) to match the resolution in the experimental spectrum. The observed line width of 180 MHz is larger than expected from the experimental resolution. With the same setup and unchanged experimental conditions, we observed a line width of less than 100 MHz for the benzonitrile monomer and of 150 MHz for the benzonitrile Ar complex. The line width observed can originate from internal effects, but experimental artifacts cannot be completely excluded. The lifetime of the S_1, 0^0 state of benzonitrile·water was measured by monitoring the total fluorescence as function of time.[37] There a value of 50 ns was found. This lifetime is far too long to explain the measured line broadening in the excitation spectrum. However, if we assume that a fast intramolecular dynamical process occurs to a state which is long-lived, the time-resolved measurement of the fluorescence then would not be able to detect the fast intramolecular dynamical process. On the other hand, line width measurements are sensitive to all dynamical processes. The existence of charge-transfer states effectively coupled to the optically accessible zero-order states was postulated from the observation of a dual fluorescence after excitation of different vibronically excited S_1 states in benzonitrile by Levy and co-workers.[38] Besides sharp emission bands, a broad feature shifted to lower energies was observed and ascribed to emission from a RICT (rehybridization by intramolecular charge-transfer) state. In very recent work, Sekiya and co-workers[39] were able to show that this broad band actually consists of a large number of sharp lines. From this they concluded that RICT states cannot account for the observed structure. However, it seems likely that the polar water molecule accelerates a charge-transfer process in the benzonitrile molecule.[40] Furthermore, it is of great interest to study the nonradiative behavior of this cluster for higher vibrational states in the S_1 excited state with high-resolution UV spectroscopy. One could expect a faster charge-transfer process with increasing excess energy in the S_1 potential leading to even larger broadening of the rovibronic transitions. Another possible origin of the line broadening could be an external perturbation. The REMPI spectra were recorded with an external electric field in the range of 50−100 V/cm in the excitation region to accelerate the ions into the mass spectrometer, a field strength known to already induce electric-field effects in benzonitrile,[41] which could also contribute to the observed line broadening.

2. Indole·Water

As a second example for a hydrogen-bonded complex, we choose the indole·water complex. We expected a different character of the hydrogen bonding from that in benzonitrile·water because of the lack of the CN group and the nitrogen atom located within the aromatic ring. This type of hydrogen bonding is important for the understanding of the stability and structure of biological systems in natural surroundings. The indole (C_8H_7N) chromophore of the amino acid tryptophan has been subject of extensive spectroscopic studies.[16,29,42−50] In the gas phase, the structure was determined by spectroscopic techniques like microwave (MW),[44] dispersed fluorescence (DF),[42] vibrationally resolved[45−47] laser-induced fluorescence spectroscopy (LIF), rotational contour LIF,[16] and rotationally resolved LIF.[48] The indole·water cluster was investigated by vibrationally resolved LIF spectroscopy and REMPI.[43,51] Two different conformers of the hydrogen-bonded indole·water complex were postulated,[42] with the water molecule acting as a hydrogen acceptor or as a hydrogen donor. The intensity of the band postulated as originating from the solvent hydrogen-acceptor (^1L_b) conformer is much larger in the measured spectra than the other origin (^1L_a). Rotationally resolved UV spectroscopy yielded the structure of the complex.[28]

First, we would like to describe the experiments performed in our group. For production of indole·water complexes, Ar gas at a backing pressure of 5 bar was mixed with water vapor of 5 mbar. The gas mixture was expanded from a heated (110 °C) reservoir of indole through a pulsed valve (modified Bosch) with a 200 μm orifice leading to a supersonic beam and the production of complexes of indole with water. Deuterated indole-d_1 was produced by solvating indole in deuterated sulforic acid and separating the deuterated indole several times.

The position of the amino hydrogen atom is determined by the analysis of the isotopically substituted indole-d_1 $S_1 \leftarrow S_0$ spectrum. The position of the water molecule is determined by the analysis of the indole·water $S_1 \leftarrow S_0$ spectrum. From a combination of both results, the bond length is calculated.

The cluster spectrum (see Figure 5) has two broad wings with a hole in the center, as is typical for a mostly *a*- and/or *b*-type transition. From this it is clear that the main inertial $a-b$ plane does not change upon attachment of the water molecule, i.e., the center of mass of the water molecule is located in the plane of indole and not above the plane of indole as in the case of benzene·water.[52−54]

The detailed analysis of this band is complicated since neither rotational constants in either electronic state nor the orientation of the dipole transition moment are available for the cluster. A CARF fit of all 12 parameters (6 rotational constants, 2 projections of the transition dipole moment on the inertial axes, electronic origin, rotational temperature, line shape, and line width) is not possible since the dimension of the problem is too large and the fitting parameters A', B', C' and A'', B'', C'' are not independent of each other. Therefore, we proceeded in an alternative way. Assuming planarity of the cluster to reduce the number of free parameters, we adapted A', B', A'', and B'' in the fit routine. C' and C'' are calculated by the planarity conditions ($1/C' = 1/A' + 1/B'$ and $1/C'' = 1/A'' + 1/B''$, respectively). The rotational temperature, the line width, and the line shape are

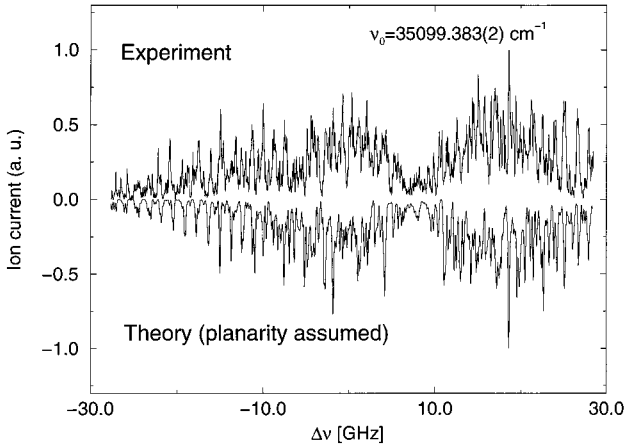

Figure 5. Upright trace: Highly resolved UV spectrum of the $S_1 \leftarrow S_0$, 0_0^0 transition of indole·water measured by mass-selected resonance-enhanced two-photon ionization. Inverted trace: Calculated spectrum assuming planarity and using the rotational constants found by the correlation automated rotational fitting (CARF) method described in section II.A.3. $\nu_0 = 35\ 099.383(2)\ cm^{-1}$ is the frequency of the band origin. (Reprinted with permission from ref 28. Copyright 1998 American Chemical Society.)

not taken as fit parameters but are fixed to reasonable values during the automatic fit procedures.

A least-squares algorithm combined with the cross correlation analysis yields the quality of the simulation shown in the lower inverted trace of Figure 5 and adapts the rotational constants within the condition of a planar complex ($1/C = 1/A + 1/B$). The agreement of line positions is quite satisfactory given the assumptions made for this planar CARF procedure. On the basis of our experimental data, we can not conclude whether a small inertial defect or a rotational line splitting (as was found by Korter et al.[30]) exist within the large error bars.

From the spectroscopic results we were able to deduce the position and structure of the hydrogen bond in the indole·water complex. The water is attached in a linear hydrogen bond between the hydrogen of the amino group and the water oxygen. The bond energy of $D_0 = 1630\ cm^{-1}$ was measured with the mass-analyzed threshold ionization technique in our recent work.[29] The center of mass of the water is basically in the plane of the indole molecule. Thus, it is clear that the indole acts as a hydrogen donor for this excitation band.

Independent measurements of the same band were performed by Pratt and co-workers using the fluorescence detection method with higher resolution.[30] They confirmed our results on the hydrogen-donor role of the indole molecule and the linear character of the hydrogen bond. Because of their better resolution they found from an autocorrelation analysis that the band is split into two bands separated by about 13 GHz and re-evaluted the value for the heavy atom separation of 3.07 Å. From this tunneling splitting they calculated that there are large-amplitude motions of the water molecule in- and out-of-plane (internal rotation and inversion or wag). The position of the water hydrogen atoms is not in the indole plane and is changed after electronic excitation from S_0 to S_1. While we did not find a change of the hydrogen-bond length within the accuracy of our mass-selective high-resolution experiments,[28] the fluorescence excitation experiments showed a small decrease of the bond length similar to the result previously found in our group for the van der Waals bonding in the benzene·Ar complex and other aromatic-molecule·noble-gas complexes.[3,17,55−57] In all systems, this is in line with the observed red shift of the $S_1 \leftarrow S_0$ transitions of the complex with respect to that of the bare molecule.

Table 3. Maximum and Mean Deviation of the Calculated Bond Lengths and Angles from the Experimental Structure of Indole in Its S_0 Electronic Ground State[44] (for details of the ab initio calculations, see text)

S_0	HF/cc-pVDZ	MP2/cc-pVDZ
$\max(\Delta_{\text{heavy atoms}})$	2.8×10^{-2} Å	5.1×10^{-2} Å
$\phi(\Delta_{\text{heavy atoms}})$	1.2×10^{-2} Å	1.4×10^{-2} Å
$\max(\Delta_{\text{hydrogens}})$	3.0×10^{-3} Å	17.0×10^{-3} Å
$\phi(\Delta_{\text{hydrogens}})$	0.9×10^{-3} Å	11.0×10^{-3} Å
$\max(\Delta_{\text{angles}})$	2.3°	2.6°
$\phi(\Delta_{\text{angles}})$	0.8°	0.9°

To shed light on this point, we calculated the structure of the indole·water cluster in the S_0 electronic ground state and its S_1 electronically excited state.[36] We computed the structure of both molecules (indole and water) with the HF and MP2 methods, which we later also used for the cluster ground-state calculations. In addition, the indole molecule was computed in its first excited-state S_1 (with single-excitation configuration interaction, CIS) while the water was calculated only in the S_0 state (with HF). This is reasonable in view of the experimental results including the electronic excitation at the indole site of the cluster. In all cases, a correlation-consistent cc-pVDZ basis set was used. To estimate the quality of our calculations, we first compared the computed structures of the indole molecule in its S_0 state with experimental data from microwave spectroscopy.[44] Table 3 summarizes the results for the deviation of the important calculated structural parameters from the experimental values. The results agree quite reasonably. However, we are aware of the fact that calculations at the same level by Callis led to an inversion of the energy order of the S_1 and S_2 state in the indole molecule.[58]

For the cluster calculation, we chose a starting geometry given by our high-resolution experiment. The water is attached to the amino hydrogen of indole with a nearly in-plane position of its center of mass. For the S_0 state calculations, we used both the HF as well as the MP2 level, while for the S_1 state calculations, CIS was applied. Throughout the cluster calculations only the six intermolecular degrees of freedom were optimized while the molecular geometries were fixed. The parameters (defined in Figure 6) of the calculated optimized cluster geometries are listed in Table 4 and compared with the experimental values of Korter et al.[30] As can be seen from Tables 3 and 4, HF theory provides better results than MP2 for the molecule as well as for the cluster. The reason for this lies in error cancellation.[59] The minimal inclusion of electron correlation in HF and the involved shortening of nonionic bond lengths is partly compensated for by the overstretching caused by

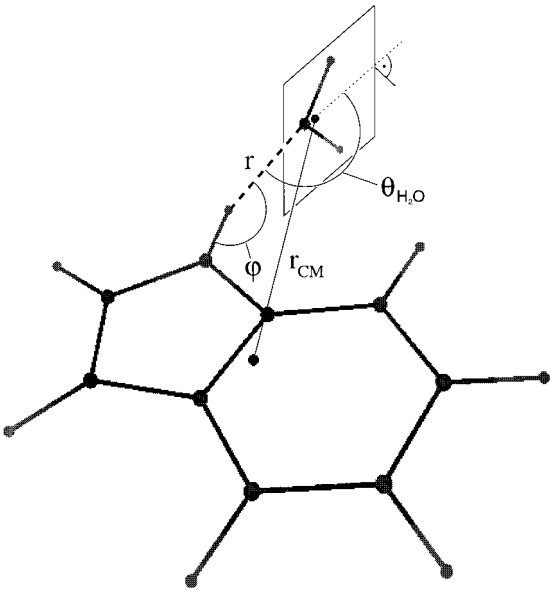

Figure 6. Structure of the indole·water complex calculated with an ab initio method at the HF level. r is the distance of the amino hydrogen from the water oxygen (hydrogen bond length); r_{CM} denotes the center of mass distances of the indole and the water molecule in the indole·water complex. $\varphi = \angle(N_I, H_I, O_{H_2O})$; $\theta_{H_2O} = \angle(COM_{H_2O}, O_{H_2O}, H_I)$.

Table 4. Calculated and Experimental Angles and Bond Lengths of the Indole·Water Cluster in the S_0 and the S_1 State[a]

	S_0			S_1	
	HF	MP2	exp[b]	CIS	exp[b]
φ	162.5°	153.7°		162.6°	
Θ_{H_2O}	154.4°	127.3°		144.5°	
Θ_I	161.2°	151.0°		160.7°	
r [Å]	2.076	1.972		2.030	
r_{CM} [Å]	4.587	4.324	4.666	4.545	4.602

[a] θ_{H_2O} = (COM_{H_2O}, O_{H_2O}, H_I) and (COM_{H_2O}, H_I, N_I). For definition of angles and bond lengths, see Figure 6. [b] Reference 30.

applying the relatively small cc-pVDZ basis set. Therefore, the HF/cc-pVDZ level seems to be a good basis for structure calculations of large systems such as indole water.

Figure 6 illustrates the structure of the cluster resulting from HF and CIS calculations. We found a nearly linear σ-hydrogen bond (see Table 4) in agreement with the experimental results of ref 30. The hydrogen atoms of water lie close to a C_s-symmetric position below and above the indole plane, while the oxygen atom lies ca. 10 mÅ outside of this plane. The disagreements between the experimental data[30] for the center-of-mass distance r_{CM} and our theoretical results for r_{CM} of 79 (56) mÅ in the $S_0(S_1)$ state might be at least partly caused by zero-point vibrational averaging in the experimental result. We find a small decrease of the hydrogen-bond length r of 46 mÅ after electronic excitation to the S_1 state and a decrease of the θ_{H_2O} angle. This originates from a horizontal internal torsion of the water plane with a movement of the water hydrogens toward the indole and not from a torsion of the water around a rotational axis outside the water molecule (see Table 4). Thus, the theoretical results are in qualitative agreement with the conclusions of the experiments of Korter et al.[30]

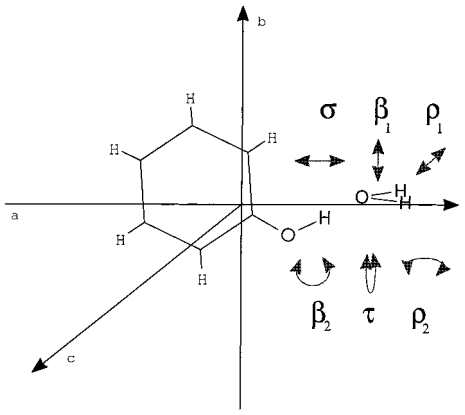

Figure 7. Structure of the phenol·water complex with the principal axis system and a schematic drawing of the motions of the water moiety for the six intermolecular vibrations. For explanation of the vibrations, see text.

C. Intermolecular Vibrational Dynamics: Phenol·Water

In the preceding sections we discussed the advantages of high-resolution UV spectroscopy for structure determination in hydrogen-bonded clusters. Once the structure is known, information on the potential is necessary for further characterization of the hydrogen bonding. The intermolecular modes provide direct access to the hydrogen-bonding potential-energy surface. As there are several large-amplitude motions of a water bound to an aromatic molecule, the intermolecular vibronic spectrum of these clusters is rather complicated. We chose a simple aromatic ring molecule with a water bound in a linear hydrogen bonding, phenol·water, to illustrate some of these issues.[14,60]

The aromatic chromophore phenol with its dipole moment and the near-UV absorption band allows the application of spectroscopic techniques for the investigation of the electronic ground state such as microwave,[61] infrared depletion spectroscopy,[62−65] Raman techniques,[66] and dispersed fluorescence[65,67] of phenol·water. The S_1 state of the cluster was investigated by vibrationally resolved laser-induced fluorescence (LIF) spectroscopy[68,69] and resonance-enhanced multiphoton ionization (REMPI).[67,70−74] The origin of the $S_1 \leftarrow S_0$ transition was investigated by highly resolved UV spectroscopy with fluorescence detection but without mass resolution.[18] The cluster ion has been investigated by zero kinetic electron energy (ZEKE) spectroscopy.[75−78] The experimentally determined structure of the phenol·water complex is shown in Figure 7 together with its inertial axes.[18,61] There is a quasilinear hydrogen bond similar to the indole·water case described above. Detailed calculations[67,79,80] are available supporting the experiments in the ionic[81] and the S_0 state of the neutral cluster, but calculations of excited electronic and vibronic states are difficult.

Phenol·water has six intermolecular modes originating from the three hindered rotations and the three hindered translations of the water molecule.

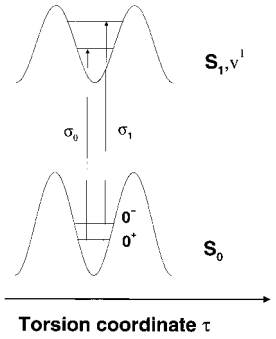

Figure 8. Transitions from the tunneling levels in the S_0 ground state to the levels of the same parity in the S_1 excited state. Note the larger tunneling splitting in the S_1, ν^1 state leading to two torsional subbands σ_0 and σ_1 in the vibronic transition.

These are illustrated in Figure 7. The two rocking modes, denoted ρ_1 and ρ_2, have a'' symmetry, the wagging modes β_1 and β_2 have a' symmetry, the torsional mode τ has a'' symmetry, and the stretching vibration σ has a' symmetry. Rotations around the free H_2O axes a, b, and c correlate with the β_2, τ, and ρ_2 modes, and the translations parallel and perpendicular to the hydrogen-bond axis correlate with σ, β_1, and ρ_1 modes, respectively. Assuming that the C_s point group of phenol·water in the S_0 state is not changed after excitation to the S_1 state, all totally symmetric (a') vibrations are allowed in the excitation process. For the nontotally symmetric vibrations (a''), the usual vibrational selection rules, $\Delta\nu = 0, \pm2, \pm4,...$, apply.

Internal rotation tunneling of the water moiety around the a axis of the complex was investigated in refs 60, 67, and 83. It has been shown[67] that the motion responsible for the tunneling splitting is a torsion mixed with the wagging vibration. We will call it torsional motion for simplicity in the following. As will be shown below, there is indeed a strong coupling between the wag and the torsion. The tunneling levels are labeled according to their parity by + and −. The − levels are at higher energy than the + levels. Interconversion of different nuclear spin species in the typical pulsed expansion time is not possible, and the statistical weights of − to + are 3:1 in phenol·H_2O. Therefore, the phenol·water complexes in the + and − torsional levels can be considered as two independent modifications of the complex. In the pure $S_1 \leftarrow S_0$ ($^1B_2 \leftarrow {}^1A_1$) electronic transition, only $+ \leftarrow +$ and $- \leftarrow -$ transitions are allowed. This is illustrated in Figure 8. Due to these selection rules, only the difference ΔE_τ in the torsional splittings in the S_0 and S_1 states are experimentally accessible. Because of the large number of intermolecular modes, their assignment is complicated.

Here, we demonstrate that rotationally resolved spectroscopy can provide additional important information for the vibrational analysis. The use of mass-selective REMPI technique with Fourier transform limited laser pulses leads to an improved signal-to-noise ratio, and weak intermolecular vibronic bands can be detected. Furthermore, if the torsional splittings are smaller than the rotational width of the vibronic bands, the spectra of the two modifications

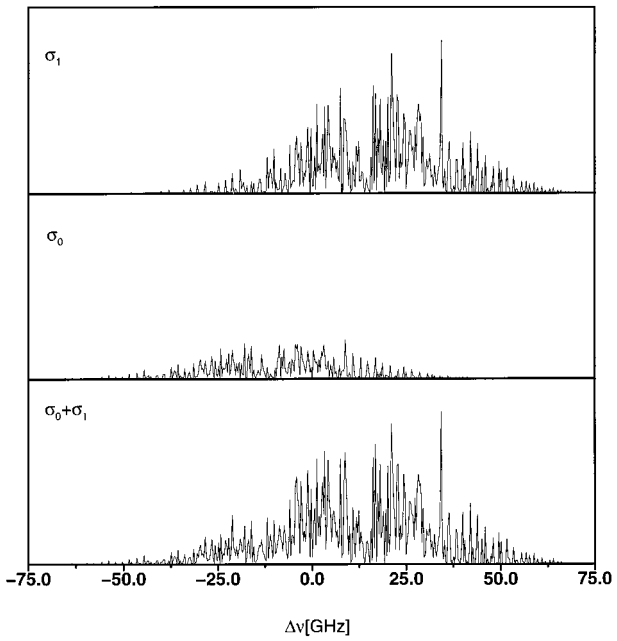

Figure 9. Schematic drawing of the two torsional subbands σ_1 and σ_0 (upper and middle trace) defined in Figure 8. Note the frequency shift of the two subbands and their different intensity. Bottom: Superposition of the two subbands with overlapping rotational contours.

of the cluster overlap. In Figure 9 a schematic drawing of the spectra of the two torsional components σ_1 and σ_0 defined in Figure 8 with statistical weight 3:1 are shown (upper two traces) together with the resulting overlapping rotational structure (bottom trace). Both contributions can be disentangled and identified only in measurements with high resolution. Here, we make full use of automated correlation techniques: First, an autocorrelation method is applied and then a fit of the rotational constants is performed with the CARF technique. From the first step we get information on torsional components in the band ,and from the second step the vibrationally averaged rotational constants are obtained which are typical for the character of the excited vibration. These techniques were applied to four intermolecular vibronic bands located within 150 cm^{-1} on the blue side of the pure electronic transition. A typical result for the autocorrelation procedure is demonstrated in the bottom trace in Figure 10. The amplitude of the autocorrelation function of the $\sigma_0 + \sigma_1$ spectrum is plotted as a function of the frequency shift between the autocorrelated identical torsional spectra. The autocorrelation function has a maximum at a given frequency difference whenever a similar pattern appears in the spectrum for this frequency shift. Indeed, the two peaks on the right and left side show clearly that two very similar rotational line patterns are present in both experimental spectra, i.e., the two torsional component spectra shown in the upper two traces of Figure 9. The central peaks in the spectra represent the band origins. The side peaks which are $\Delta E_\tau = 0.85$ cm^{-1} apart in the 0_0^0 band from the center have $^1/_3$ of the intensity of the central peaks. The appearance of the two symmetric side peaks originates from the principal symmetry of the autocorrelation function. It is direct evidence

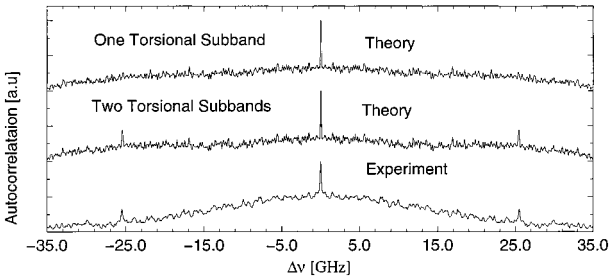

Figure 10. Autocorrelation of the $S_1 \leftarrow S_0$, 0_0^0 spectrum of phenol·water shown in Figure 9. Top: Theoretical trace for one torsional subband. Middle: Theoretical trace for two torsional subbands. Bottom: Experimental trace. The side peaks appear only in the middle and bottom graphs. The band consists of two torsional subbands. For details, see text. (Reprinted with permission from ref 60. Copyright 1998 American Institute of Physics.)

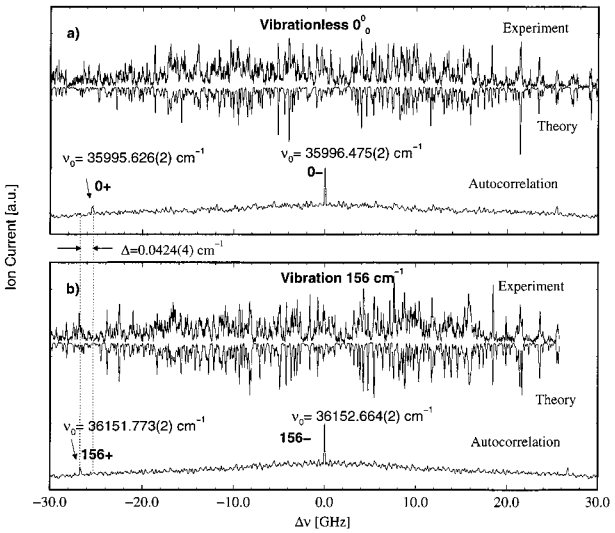

Figure 11. (a) Rotationally resolved $S_1 \leftarrow S_0$, 0_0^0 transition of phenol·water. From top to bottom: Experiment, theory (inverted), and autocorrelation of the experimental trace. The small peaks of the autocorrelation trace reveal the position of the second torsional subband 0^+. (b) Rotationally resolved spectrum of the $S_1 \leftarrow S_0$, 156 cm^{-1} vibronic band. From top to bottom: Experiment, theory (inverted), and autocorrelation of the experimental trace. The autocorrelation reveals the second torsional subband 156^+. The difference of the energy splitting Δ is an indication for the coupling between the torsional and the 156 cm^{-1} stretching mode. (Reprinted with permission from ref 60. Copyright 1998 American Institute of Physics.)

for the existence of two overlapping torsional transitions with very similar rotational structure in the two bands. The energy difference of the two transitions can be directly found from the autocorrelation function with high accuracy without any assignment of the rotational structure of the spectra. For comparison, in Figure 10 the theoretical autocorrelation function is shown when calculated for spectra with one (top trace) and two (middle trace) different subbands. The good agreement of the theoretical spectrum in the middle trace of Figure 10 with the experimental one at the bottom of Figure 10 shows that the side peaks in the experimental autocorrelation can only be explained by the second subband. The sign and the confirmation of the energy splitting is obtained from the detailed analysis of the spectrum (see below). This is demonstrated in Figure 11, parts a and b, where two vibronic bands are presented above each other with their simulation and autocorrelation functions. Identical features are recognized, and the difference of torsional splitting ΔE_τ of both bands can directly be read off.

The rotational constants obtained from a simulation of the spectrum with the CARF procedure are listed in Table 5. The values of the rotational constants of the 0^+ and 0^- levels agree with the results of Berden et al.[18] Torsional splittings with overlapping rotational bands are found for the electronic origin (0^+,0^-) and the band at 156 cm^{-1} (156^+, 156^-) (see Figure 11). The latter shows a torsional splitting of about the same magnitude as the 0_0^0 band and is assigned to the intermolecular stretching vibration. Bands with a single torsional component are located at 95 and 121 cm^{-1} excess energy. To identify the character of these bands, a comparison of the rotational constants is useful. The differences in the individual rotational constants of the investigated bands from that of the pure electronic transition are illustrated in Figure 12. It is clearly seen from the values of the 0^+, 0^- and the 156^+, 156^- bands, respectively, that the two torsional components of a single vibronic band have similar rotational constants. As the rotational constants of the bands at 121 and 125 cm^{-1} excess energy are equal to each other, we conclude that they represent two torsional components of a single vibronic band. They appear as individual bands under high resolution; their parity is assigned on the basis of the results in ref 82. The most striking result of Figure 12 is that the band at 95 cm^{-1} excess energy has a very different rotational constant *A*, much larger than that

Table 5. Rotational Constants of Various Vibronic Bands in the Phenol·Water Cluster Obtained with the CARF Method[a]

	0+	0−	95+	121−	125+	156+	156−
A″ [MHz][b]	4291.49(4)	4281.76(1)	4291.49(4)	4281.76(1)	4291.49(4)	4291.49(4)	42 81.76(1)
B″ [MHz][b]	1092.1445(2)	1092.3254(1)	1092.1445(2)	1092.3254(1)	1092.1445(2)	10 92.1445(2)	1092.3254(1)
C″ [MHz][b]	873.7271(2)	873.9082(1)	873.7271(2)	873.9082(1)	873.7271(2)	873.7271 (2)	873.9082(1)
ΔI″ [amu Å^2]	−2.086(1)	−2.3968(6)	−2.086(1)	−2.3968(6)	−2.086(1)	−2.086(1)	−2.3968(6)
A′ [MHz]	4186.8(1)	4171.9(5)	4317.7(9)(4)	4182.7(2)	4208.2(21)	4170.6(7)	4158.8(5)
B′ [MHz]	1099.5(2)	1100.4(2)	1097.9(5)	1101.3(1)	1094.5(6)	1093.2(6)	1094.5(3)
C′ [MHz]	873.748(7)	874.69(8)	873.6(4)	873.8(2)	871.5(2)	870.1(3)	870.54(3)
ΔI′ [amu Å^2]	−1.95(8)	−2.6(1)	1.2(3)	−1.35(1)	−1.9(3)	−2.6(3)	−2.7(1)
E_0 [cm^{-1}]	35995.626(2)	35996.475(2)	36090.526(2)	36117.022(2)	36121.618(2)	36151.773(2)	36152.664(2)
ΔE_0 [cm^{-1}]	0	0.8491(2)	94.900(3)	121.396(3)	125.992(3)	156.147(3)	157.038(3)

[a] ΔI, inertial defect; E_0, transition frequency; ΔE_0, frequency shift from the electronic origin. [b] Reference 61.

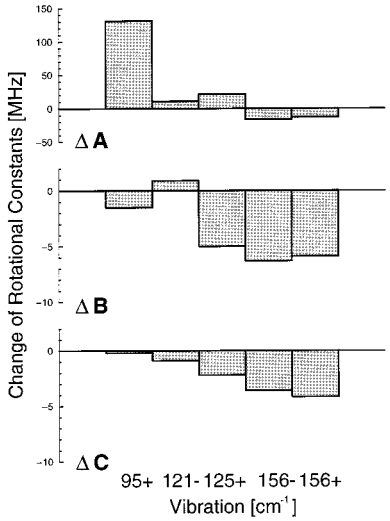

Figure 12. Top: Change of rotational constants in various final vibrational states in the S_1 state of phenol·water relative to the vibrationless level. Note the different behavior of the 95^+ vibration. For explanation, see text.

of the other bands. Therefore, the assignment of a vibration with strong coupling is very likely pointing to a torsional character of this band.

From the torsional splittings and the measured rotational constants we make the following assignments.

1. Stretching Mode σ: 156⁺, 156− cm⁻¹

The energy distance of the torsional subbands of $\Delta E_\tau = 0.8915(3)$ cm^{-1} of this band is similar to the splitting of the vibrationless $S_1 \leftarrow S_0$, 0_0^0 transition of 0.8491(2) cm^{-1} (see Figure 11). The slight increase of the splitting by only 5% demonstrates that the excited vibrational mode is only slightly coupled to the torsional mode as expected for a stretching vibration. The small decrease of the rotational constants B' and C' and the larger decrease of A' is also in line with the assignment as a stretching mode (see Figure 12). The decrease of A' is the result of the averaged vibrational motion preferentially along the a axis, which is expected for a stretching vibration.

2. Wagging Mode β₂: 121−, 125⁺ cm⁻¹

We tentatively assign the 125 cm^{-1} band as the β_2^+ transition. Their similar rotational constants (see Figure 12) clearly support the assignment of the 121 and 125 cm^{-1} bands as two torsional subbands of a single vibration. The resulting large torsional splitting of $\Delta E_\tau = -4.596(3)$ cm^{-1} points to a strong coupling of the excited wagging vibration with the torsional motion. The coupling changes the torsional barrier and the torsional splitting. The strong coupling is in good agreement with calculations in the intermolecular $\tau-\beta$ potential surface[67] and in line with the assignment as the first quantum of the wagging mode. This tentative assignment of the 125 cm^{-1} band as the β_2^+ component is at variance with previous work,[67,75] where the two bands at 121 and 125 cm^{-1} were assigned to two different vibronic transitions and the 121 cm^{-1} band has been assigned as a complete β_2 vibration.

There is one point in contradiction with the splitting of −4.596(3) cm^{-1} originating from the β_2^+ assignment: The torsional barrier in S_0, 0_0 is about 150 cm^{-1}, resulting in an absolute splitting of less than 2.5 cm^{-1}. In S_1, 0^0 the barrier is 120 cm^{-1}, leading to an absolute splitting of less than 3.5 cm^{-1}.[18,67,82] The absolute splittings were confirmed by ZEKE experiments,[75] where the transitions to the ionic cluster are measured. To be in line with a splitting *difference* of −4.6 cm^{-1} between S_0, 0_0 and S_1, β_2, the absolute order of the two lowest states in the torsional potential S_1, β_2 must be inverted and the lowest state in this torsional potential must have negative parity with respect to the exchange of the hydrogen atoms. This does not agree with fundamental rules of quantum mechanics. Insisting on the β_2^+ assignment would result either in an absolute ground-state splitting larger than 4.6 cm^{-1} or a change of the parity selection rules from $+ \leftarrow +$ and $- \leftarrow -$ to $+ \leftarrow -$ and $- \leftarrow +$, respectively. A change of the selection rules could be explained by a symmetry change in S_1, β_2, similar to the case of H_2-C=O.[84] This geometry change would lead to a change of the rotational constants which is not found. Another possible explanation accounting for the splitting difference could be the influence of the water rotation on the excited bending motion. On the other hand, the β_2^+ assignment is supported by the similarity of the rotational constants, the intensity ratio, and the parity of the two transitions. Further experimental and theoretical investigations should clarify this point.

3. Torsion τ: 95 cm⁻¹

The 95 cm^{-1} band has been assigned differently. The ZEKE double-resonance experiments[75] and calculations[82] suggest an assignment as a transition to a torsional level. As pointed out above, the measured value of the rotational constants of the excited vibration (see Figure 12) shows a large change of the constant A', different from the pattern of the other vibrations. This points to a strong coupling of the excited vibration at 95 cm^{-1} supporting the assignment as the torsional mode or one of its higher harmonics. Our spectra show just one torsional component in the measured spectral range.

From a comparison of the intensity of the 95 cm^{-1} band with the intensity of the neighboring bands,[75] we conclude that the 95 cm^{-1} band represents the higher intensity + parity component. Thus, the vibrational state at 95 cm^{-1} is an overtone of the torsional vibration with + parity.

In conclusion, high-resolution UV spectroscopy with Fourier transform limited laser pulses enables one to detect weak intermolecular vibronic bands and resolve their rotational structure. For the example of phenol·water, high-resolution UV spectroscopy provides information for a reasonable assignment of three vibronic bands with their torsional components. While the intermolecular stretching vibration is only weakly coupled with the torsional motion of the water molecule (torsional splitting 0.8015(3) cm^{-1}), the wagging motion is strongly coupled leading to a large torsional splitting of −4.596(3) cm^{-1}. Finally, the band at 95 cm^{-1} is assigned to the pure torsional transition or, more likely, to the second overtone.

III. Cationic Clusters

A. General Remarks

The vast majority of spectroscopic information on larger polyatomic molecular systems and in particular on clusters is restricted to neutral systems (see section II). Ionic clusters are expected to possess properties differing from those of their neutral counterparts due to the stronger binding and often radical character of the ionized cluster constituent. This means that information existing for the neutral clusters cannot be naively used to describe the ionic system and direct measurements of the ionic clusters are necessary. The difficulties in producing cold ionic complexes by electron impact, discharge, capture in matrices, and storage in traps have restricted investigations with conventional high-resolution microwave, IR, or UV spectroscopy to small molecules and clusters thereof,[85,86] whereas high-resolution work on polyatomic molecular ions is sparse. Partly rotational resolution was achieved in laser-induced fluorescence experiments on the hexafluorobenzene cation,[87] though small effects leading to an observed broadening of the transitions were not resolved.

In this review, recent advances of a technique avoiding the difficult production of ionic clusters prior to high-resolution experiments are described. This technique is based on the excitation and resolution of high n ($40 \lesssim n \lesssim 110$) Rydberg states in the *neutral* molecule or cluster prior to pulsed field ionization and detection of the resulting ions in a time-of-flight mass spectrometer. If there is negligible interaction of the highly excited Rydberg electron with its cluster core, the vibrational and rotational energies of the ionic core exhibit themself in a shift in energy of the Rydberg series and their limit for $n \rightarrow \infty$. Different Rydberg series are characterized by their ionization energy and quantum defect. By detecting the limits of the Rydberg series with a special computer-assisted method, the rotational energy levels of the cation can be determined with high accuracy.[88] This method is different from the experimental techniques of zero kinetic electron energy spectroscopy (ZEKE)[89,90] and mass-analyzed threshold ionization spectroscopy (MATI),[91,92] which are based on the excitation of very high unresolved Rydberg states and an electric field extrapolation. Here the extrapolation to the energy levels of the cationic states is performed using the Rydberg formula and the energy positions of the individual, resolved Rydberg states in the range $n \approx 40-110$.[88] The a priori unknown quantum defect of each Rydberg series can be taken into account by including numerous members of an individual Rydberg series in the analysis.

While the resolution achieved in ZEKE and MATI experiments is limited to cluster vibrations, the technique of resolved high Rydberg spectroscopy offers rotational resolution where even deviations caused by small effects, e.g., spin−orbit coupling effects of the remaining unpaired electron in the chromophore, can be measured (see below).[93] Mass selection is achieved by ion detection, a feature which is essential when examining clusters.

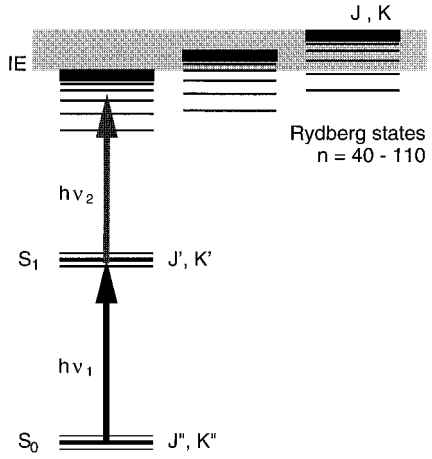

Figure 13. Double-resonance excitation scheme of high Rydberg states with subsequent pulsed-field ionization used in the present experiment. The first laser frequency (ν_1) is fixed to a selected transition from the electronic ground-state S_0 with rotational quantum number $J''_{K''}$ to the intermediate state S_1, $J'_{K'}$. The second laser frequency (ν_2) is scanned over the range of the high Rydberg states closely below the first ionization energy of the cluster. The different Rydberg series converge to the rotational levels J, K of the cluster cation in its vibronic ground state.

B. Experimental Setup

Excitation of high n Rydberg states of polyatomic molecules and their clusters with noble gases requires a double-resonance excitation scheme using a rovibronically selected intermediate state state of the molecule or cluster. Figure 13 illustrates this excitation scheme. The experimental setup is based on the one used for the investigation of neutral clusters with highly resolved UV spectroscopy (see section II.A.1). Double-resonance excitation requires the replacement of the broad band dye laser used for the ionization step by a second narrow band UV-laser setup similar to the one used for the first excitation step; i.e., the preparation of the intermediate state. It is additionally equipped with an autoscan system (Coherent Autoscan) to make scans feasible over wide frequency ranges of several 10 cm^{-1}. The high Rydberg states are ionized by a delayed pulsed electric field and subsequently detected in the time-of-flight mass spectrometer. The delay time is about 20 ns in the present experiments to avoid accidental time overlap of the laser pulses and the pulsed ionization field, ensuring laser excitation under field-free conditions. To minimize residual electric stray fields, the ion optics were covered with graphite.

For some experiments (see section III.G), a more sophisticated electric field pulse scheme was used to allow the separation of prompt ions produced during laser excitation and the neutral high Rydberg states prior to pulsed field ionization of the latter. The pulse scheme used is similar to that of MATI experiments and necessary when examining high Rydberg states above the lowest ionization threshold. A small separation field of 0.5−3 V/cm is applied for a duration of 4−45 μs and followed by the pulsed field for ionization of typically 180 V/cm. The mass resolution achieved in this pulsed mode is somewhat smaller

than in the UV spectroscopy experiments on neutral clusters but still sufficient to discriminate the different cluster species present in the molecular beam.

C. Individual Rydberg States and Their Dynamics in Clusters

Spectroscopic investigations of molecular Rydberg series have been an important source of information about the character and dynamics of higher excited electronic states.[94,95] In contrast to valence states, Rydberg states show a regular energetic spacing described by the well-known Rydberg formula, allowing the extrapolation of the ionization energy from the position of single Rydberg states. Excitation of individual Rydberg states is realized by double-resonance excitation via an intermediate state in the first electronically excited S_1 state of the molecules. For a rotational analysis, it is required to resolve a single rovibronic state in the intermediate state S_1 in order to prepare a selected initial state with known rotational quantum numbers $J'_{K'}$. This is an important precondition for application of this method on clusters with very dense electronic structure. In the second excitation step, high Rydberg states lying just below the lowest ionization threshold of the molecule or cluster are excited using a second, narrow band laser pulse (see Figure 13). For the first time resolved high Rydberg state spectra in polyatomic molecules were reported for the prototype system benzene in the range $45 \lesssim n \lesssim 110$.[96] The measured minimum peak width of the Rydberg states is 400 MHz and increases with the principal quantum number n. The range of resolvable individual Rydberg states to very high n's is restricted by the congestion of the Rydberg series. It leads to a permanent overlap of Rydberg states belonging to different Rydberg series. Under common experimental conditions, this limit is around $n \approx 100$. In the first experiments on van der Waals clusters of benzene with noble gases, individual Rydberg states were resolved in an n range comparable to that of the benzene monomer.[97] The lifetimes of the Rydberg states observed are tens of microseconds, so that suitable ion separation techniques can be used.

It is well accepted that l and l,m splitting and mixing of the Stark states in residual electric stray fields and external electric fields is mainly responsible for the observed long lifetimes of high Rydberg states with $n > 45$ in the microseconds range.[98−104] While Stark mixing within the residual electric stray field leads to an overlap and a complete mixing of the Rydberg states in the very high n range ($n > 150$) used for ZEKE and MATI techniques, the broadening in the $45 \lesssim n \lesssim 110$ range does result in a broadening of about 400 MHz but not in an overlap of the individual n Rydberg states. The investigations of resolved high Rydberg states in benzene[88] yielded a resolution of 0.012 cm^{-1} and enabled us to study the influences of external electric fields on the width and decay time of individual Rydberg states. One major result of this study was the finding that the decay is nonuniform within the shape of a single Rydberg peak. Also, the peak shape varies substantially with different applied external fields.[88,105]

Thinking about high Rydberg states of van der Waals clusters, the question arises whether ionic cores with large dipole moments and low frequency vibrations may lead to hitherto unobserved Rydberg−core coupling and a reduced Rydberg state lifetime.[106,107] Cationic van der Waals complexes possess an exciting feature for studies of Rydberg−core coupling, pointing out the theoretical challenges associated with the vibronic coupling of Rydberg states and core motions. Cationic aromatic-molecule·rare-gas complexes combine the properties of a strongly localized charge at the aromatic chromophore and large charge separation from the center of mass. The center of mass of the cluster does not coincide with the center of charge, leading to a strong dipole moment. Therefore, any rotational or vibrational motion of the cluster core leads to large time-dependent displacements of the spatial origin of the Coulomb potential because the Rydberg wave function has to follow the moving center of charge. For fast moving electrons, this problem can be treated in the Born−Oppenheimer approximation. However, for high n Rydberg states above $n = 50$, the time scales for intermolecular vibrations, overall rotations, and Rydberg orbits are comparable and no simple separation of time scales is possible.

The same problem can be described in a different way, which clearly shows the differences between clusters and atomic and most molecular systems. If we want to retain the fixed origin of the Coulomb potential at the center of mass, the electrostatic potential has to be expanded in multipole moments with respect to the center of mass. This leads to a monopole at the center of charge and strong time-dependent rotating and vibrating multipole moments.[107,108] Typical dipole moments at the equilibrium position are about 4 D for benzene$^+$·Ar and 6 D for benzene$^+$·Kr, for the large distances of 3.5 Å between the centers of mass of the cluster components. Therefore, because of the high density of rotational states of clusters, it was argued that resonant vibronic couplings between series converging to different vibrational or rotational core states perturb the energetic $1/n^2$ Rydberg structure completely and destroy the simple picture of uncoupled electronic and core motion.

We were able to shed light on this question in the present experiments:[93,97,109] The upper trace in Figure 14 shows a overview Rydberg spectrum of the benzene·Ne cluster in the range $60 \lesssim n \lesssim 130$ measured via a selected rotational state in the S_1, 6^1 intermediate state. The inset on top of Figure 14 shows part of the experimental (upright trace) and theoretical (inverted trace) spectrum on an enlarged scale. The typical width of a single Rydberg state in this spectrum is 600 MHz. The spectrum contains five different Rydberg series converging to five different rotational states of the cationic ground state. Similar spectra were recorded for the clusters of benzene with the heavier rare-gas atoms Ar and Kr. The spectra can be simulated (see lower inverted trace of Figure 14) using the Rydberg formula with a zero quantum defect and the series limits of the Rydberg series found from the experimental spectra.

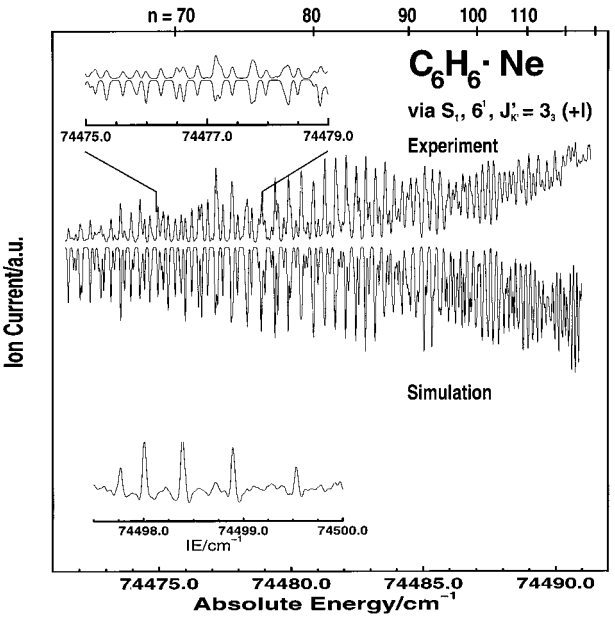

Figure 14. Upper trace: Measured Rydberg spectrum converging to rotational states in the vibrational ground state of the benzene^{+}·Ne cluster cation. Lower inverted trace: Simulated spectrum consisting of an unperturbed superposition of five Rydberg series with different intensities converging to the series limits found in the cross correlation analysis (see text). The inset in the top part of the figure shows a detailed view demonstrating the good agreement of the measured and the simulated Rydberg spectra. The *n* values given on the top side of the frame refer to the strongest series. The inset in the lower part of the figure shows the cross correlation of the measured spectrum with simulated Rydberg series presenting the series limits of the overlapping Rydberg series.

(For the evaluation of the series limits, see bottom trace of Figure 14 and section III.D.) The intensity of the simulated series is fit to the experimental spectrum. Similar to the benzene Rydberg spectra,[88] the widths of single Rydberg peaks increase with *n*. Therefore, the peak width is attributed to Stark broadening within the residual electric stray field which is estimated from the observed peak widths to be less than 100 mV/cm. Rydberg states can be resolved up to about $n \approx 100$; at higher *n* the congestion of the Rydberg series leads to permanent overlap of the single *n* Rydberg states.

The assignment of individual peaks enables us to check for strong vibronic perturbations of the Rydberg series expected from the theoretical prediction above. However, no perturbations were found within the resolution of the experiment, mainly given by the Stark width of the individual Rydberg states caused by the residual stray field. The energetic positions are described very accurately by the Rydberg formula and all observed series show a vanishing quantum defect and no observable local perturbations of the frequency positions. As mentioned above, this is surprising in view of the possible resonant couplings between core rotation and electron orbit as suggested by the similar classical time-scales of motion.[106] A coupling between intermolecular vibrations and Rydberg series is not probable in the observed region. Its existence could be checked in an energy range well above the lowest ionization level where the density of van der Waals vibrations of the cluster is high enough to allow for resonances between Rydberg states belonging to different van der Waals modes in the higher *n* range.

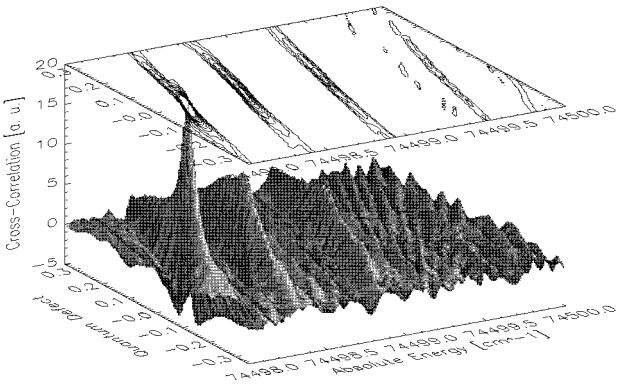

Figure 15. Three-dimensional representation of the cross correlation spectrum (CRIES) of the Rydberg series of the C_6H_6·Ne cluster measured via the S_1, 6^1, $J'_{K'} = 4_4$ intermediate state as a function of the absolute energy of the series limits and the quantum defect δ. Note that the maxima of the CRIES function are located at $\delta = 0$. Local maxima along the energy axis represent rotational state energies of the cationic ground state of $C_6H_6^{+}$·Ne.

D. Extrapolation of Rydberg Series

Assigning the individual Rydberg states to different series and their extrapolation to the respective series limits determines the rotational state energies of the cationic clusters with high accuracy. A quantum defect can easily be included in the analysis because of the large number of individual Rydberg states per series present within a spectrum. However, the high density of states in the Rydberg spectrum of van der Waals clusters makes an assignment of the individual Rydberg peaks to the different series difficult and easily subject to errors. To avoid these difficulties, an automated computer-assisted method for the determination of the series limits was developed and applied.[88] The technique is based on the fact that the appearance of a regular Rydberg structure in a certain energy range of the experimental spectrum corresponds to a local maximum in the cross correlation function between a simulated Rydberg series and the experimental spectrum. To obtain a fast method suitable for laboratory use, we use the *discrete convolution theorem*[21] for calculation of the cross correlation spectra (as in the computer-assisted assignment technique of section II.A.3). In the implementation of this method, the calculation of cross correlation spectra for a given quantum defect needs three fast Fourier transform calculations and a vector multiplication and can be completed in 1 s on a personal computer. This method has been referred to as cross correlation ionization energy spectroscopy (CRIES).[88] By varying the quantum defect of the test Rydberg series, a three-dimensional plot of the cross correlation function as a function of the ionization energy ν_{J_K} and the quantum defect δ is obtained. Figure 15 shows such a three-dimensional CRIES spectrum obtained from a measured Rydberg spectrum of C_6H_6·Ne measured via the S_1, 6^1, $J'_{K'} = 4^4(+l)$ intermediate state. The contour plot on top shows the maxima of

the cross correlation at vanishing quantum defect ($\delta \approx 0$). The resultant widths of the CRIES peaks in a two-dimensional cut of such a plot are given by the average peak widths of the Rydberg states of the corresponding Rydberg series. We found that the quantum defect of all detected Rydberg series in benzene·rare-gas clusters are zero within the accuracy of the experiments. Therefore, we used two-dimensional cuts at the quantum defect $\delta = 0$ for the analysis of the cationic rotational states. As an illustration, the inset in Figure 14 shows the CRIES spectrum of the measured Rydberg spectrum of C_6H_6·Ne. The five peaks found in the CRIES spectrum picture the five Rydberg series present in the experimental spectrum converging to different rotational states of the cationic ground state of the cluster.

E. Structure of Cationic Benzene$^+$·Rare-Gas Clusters

1. $C_6H_6^+$·^{20}Ne

The series limit of an individual Rydberg series represents a rotational state of the cationic cluster in its vibronic ground state. Using the CRIES technique (see section III.D), these series limits are determined in an automated way by cross correlation even for the very dense Rydberg spectra of aromatic-molecule·rare-gas clusters (see Figure 15 and top of Figure 17). By measuring Rydberg spectra via several different intermediate states, sufficient data for a rotational analysis can be collected. The series limits found in the Rydberg spectra measured for benzene·Ne have been published elsewhere.[110]

In their neutral S_0 (S_1) states, the benzene−rare-gas clusters are rigid prolate symmetric rotors with the rare-gas atom centered above the benzene ring at a distance of 3.45 (3.41) Å in benzene·Ne.[55] The recent investigation of the benzene molecular cation by resolved high Rydberg spectroscopy showed that the rotational spectra of the cationic monomer can be treated as that of a symmetric rotor with high accuracy.[88] In the benzene rare-gas van der Waals clusters, the benzene ring is the light-absorbing chromophore of the cluster and ionization occurs at the benzene site because of the much higher ionization energy of the rare-gas atom. The energy levels of a rigid symmetric rotor include a Coriolis-type term, made necessary because of the electronic degeneracy of the $\tilde{X},^2E_2$ state in point group C_{6v}. These are given by[111]

$$E_{NK(\pm l)} = \nu_0 + BN(N+1) + (A-B)K^2 \pm 2A\zeta_{\mathrm{eff}}K \quad (1)$$

Here, $E_{NK(\pm l)}$ represents the series limit (and thus the rotational state of the cationic core) and ν_0 denotes the adiabatic ionization energy of the cluster. The sign of the last term in eq 1 depends on the Coriolis component ($\pm l$). The rotational constants A, B, the Coriolis coupling constant ζ_{eff}, and the adiabatic ionization energy ν_0 were fit to the experimental data. As a result we found the structure of the benzene$^+$·Ne cluster cation with the Ne atom centered above the benzene ring as in the neutral states (see Figure 16). The distance of the Ne atom from the center of mass of the benzene ring was evaluated using the Kraitchman equation.[112] The average distance of the Ne atom is found to be $\langle r \rangle = 3.320(2)$ Å. The rotational constants of benzene$^+$·Ne and its adiabatic ionization energy ν_0 are listed in Table 6. Though no Jahn−Teller splitting of the zero-point level of the benzene$^+$·Ne cluster is expected, the quadratic Jahn−Teller effect is known to lead to three potential minima around the 6-fold degenerate rotational axis with their depths depending on the strength of the quadratic Jahn−Teller coupling.[111] Calculations of the coupling constants have shown that these minima are shallow. Thus, the zero-point vibrational level should be above the resulting barrier, leading to an effective 6-fold symmetry axis.[113,114]

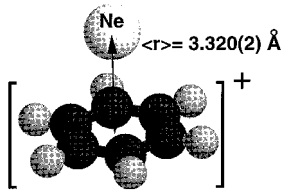

Figure 16. Experimental structure of the $C_6H_6^+$·^{20}Ne cluster cation. The position of the Ne atom is above the benzene ring on the C_6 axis at an average distance of $\langle r \rangle = 3.320(2)$ Å. (Reprinted with permission from ref 109. Copyright 1998 Elsevier Science.)

The change in the benzene ionization energy due to complexation is equal to the differences in the van der Waals binding energy between the neutral and ionic ground state of the cluster. Thus, the determination of the ionization energies with resolved high Rydberg spectroscopy provides an accurate value of the difference in binding energy of the Ne atom to the benzene molecule (see Table 7). For determination of the absolute binding energy, the dissociation energy of the cluster has to be measured, e.g., with the MATI technique.[115]

2. $C_6H_6^+$·Ar and $C_6D_6^+$·Ar

In their neutral S_0 (S_1) states, C_6H_6·Ar and C_6D_6·Ar are rigid symmetric tops with average distances of the Ar above the benzene ring of 3.58 Å (3.52 Å) for both the benzene isotopomers. The series limits found with resolved high Rydberg spectroscopy (see middle trace in Figure 17), and their assignments to the cation rotational states are made available elsewhere.[110]

Table 6. Rotational Constants of the Benzene$^+$·X (X = ^{20}Ne, Ar, ^{84}Kr) Cluster Cations and Corriolis Coupling Constant ζ_{eff} in their Zero-Point Vibrational Level. Absolute Energy ν_0 of the $J = 0$ Rotational Level for an Assumed Vanishing Spin−Orbit Coupling Constant

	$C_6H_6^+$·^{20}Ne	$C_6H_6^+$·Ar	$C_6D_6^+$·Ar	$C_6H_6^+$·^{84}Kr
origin [cm^{-1}]	74497.513(9)	74386.783(18)	74414.748(14)	74325.226(14)
B [cm^{-1}]	0.06346(24)	0.0405(6)	0.0383(5)	0.0268(5)
A [cm^{-1}]	0.0943(9)	0.0924(33)	0.0775(13)	0.0939(24)
ζ_{eff}	0.465(14)	0.441(45)	0.439(28)	0.428(22)

Table 7. Average Distance $\langle r \rangle$ of the Rare-Gas Atoms from the Center of the Benzene Ring in the Cationic Ground State $\tilde{X}$ and Respective Values for Their Neutral S_0 and S_1, 6^1 States.[17,57] Increase of the van der Waals Binding Energy ΔE_{Bind} in the Neutral S_1, 6^1 and the Cationic $\tilde{X}$ States (taken from ref 93)

		C_6H_6·^{20}Ne	C_6H_6·Ar	C_6D_6·Ar	C_6H_6·^{84}Kr
$\langle r \rangle$ [Å]	S_0	3.454(1)	3.581(1)	3.578(1)	3.676(1)
	S_1, 6^1	3.415(3)	3.521(2)	3.519(2)	3.607(1)
	$\tilde{X}$	3.320(2)	3.513(3)	3.497(3)	3.651(3)
ΔE_{Bind} [cm^{-1}]	S_1, 6^1	+2.87(1)	+21.018(15)	+20.771(15)	+33.397(15)
	$\tilde{X}$	+59.06(3)	+169.771(30)	+168.759(30)	+231.349(30)

Table 8. Spin−Orbit Coupling Constants *a* of Benzene$^+$·X (X = ^{20}Ne, Ar, ^{84}Kr) Cations Measured with Resolved High Rydberg Spectroscopy. Note the Increasing Values with Increasing Mass of the Noble-Gas Atom (for explanation, see text)

	$C_6H_6^+$·^{20}Ne	$C_6H_6^+$·Ar	$C_6D_6^+$·Ar	$C_6H_6^+$·^{84}Kr
a [cm^{-1}]		0.52(12)	0.51(9)	2.94(24)

The analysis of all ionic states shows that states with $K > 0$ and higher values of N fit nicely into the picture of a rigid prolate symmetric top represented by eq 1. In contrast, states with $K = 0$ and the low $N,K = 1$ states are split into two components or slightly shifted in their position. These effects are equal for protonated and deuterated benzene$^+$·Ar. An asymmetric top structure of the cluster after ionization would cause a splitting of $K = 1$ levels which would increase with N.[111] Other possible mechanisms, e.g., l-type doubling, j-type doubling, either increase with increasing N or are not expected to affect states with $K = 0$. The extensive treatment of rotational levels of symmetric top molecules in degenerate ^2E states by Brown[116] includes the possibility of first-order spin−orbit coupling effects by a phenomenological form of the spin−orbit interaction operator suggested by van Vleck[117]

$$H_{so} = a\mathbf{L}\cdot\mathbf{S} \tag{2}$$

where a is the spin−orbit coupling constant. Diagonalization of the Hamiltonian matrix leads to an equation of the eigenvalues for the rotational states including the effects of first-order spin−orbit coupling. Considering a Hund's case (b) equivalent case with weak coupling of the spin to the top axis, it was shown that only levels with the same value of K mix together. Therefore, K remains a good quantum number and the energy levels of a symmetric top molecule including the effect of first-order spin−orbit coupling are given by

$$E_{\pm} = \nu_0 + B\left(J + \frac{1}{2}\right)^2 + (A - B)K^2 - 2A\zeta_{eff}K + A\zeta_{eff}^2 \pm \frac{1}{2}B\sqrt{(Yd)^2 - 4KYd + (2J+1)^2} \tag{3}$$

with $Y = a\zeta_{eff}/B$ and $d = \pm 1$. Setting $Yd = 0$, $J = N - {}^1/_2$ for the E_+ component and $J = N + {}^1/_2$ for the E_- component in eq 3; eq 3 reduces to eq 1. E_+ is called an F_2 component ($J = N - {}^1/_2$) and E_- an F_1 component ($J = N + {}^1/_2$). Note that eq 3 describes four degenerate pairs of distinct eigenvalues since $K = \pm|K|$, $d = \pm 1$ and $\zeta_{eff} = \pm|\zeta_{eff}|$. Special treatment is necessary for the case where $J = |K| - {}^1/_2$, i.e., $K = \pm(J + {}^1/_2)$. In this case there are no states with smaller J to mix with. K is subject to the limitation $|K| \le N$, and therefore, these states must be F_2 states. Brown[116] gives the expression

$$E_+ = \nu_0 + B|K| + A(K^2 + \zeta_{eff}^2) \mp a\zeta_{eff}d/2 - 2A\zeta_{eff}K \tag{4}$$

for these cases. The upper or lower sign refers to $K = \pm|K|$, respectively.

The constants B, A, ζ_{eff}, the spin−orbit coupling constant a, and the origin of the rotational spectra ν_0 were fit to the experimental data. The very good agreement with the theoretical model of eqs 3 and 4 proves that the observed splitting is caused by spin−orbit coupling of the single unpaired electron in benzene$^+$. The spin−orbit coupling in the benzene$^+$·Ar cluster cation is stronger than in the benzene cation monomer and the benzene$^+$·Ne cluster and is therefore ascribed to an external heavy atom effect (see section III.F). The fitted values of the constants are summarized in Table 6, and the spin−orbit coupling constant is included in Table 8. All observed rotational levels have $d = -1$. (Note that ν_0 here does not correspond to the adiabatic ionization energy since according to eq 4 the lowest states observed are shifted to lower energy than that of ν_0.) The deduced values for the average distances of the Ar atom in the cluster and the shifts in the van der Waals binding energy (see section III.E.1) are given in Table 7.

3. $C_6H_6^+$·^{84}Kr

Assuming that the observed effects of spin−orbit coupling on the rotational levels of the benzene$^+$·Ar clusters are caused by the external heavy atom Ar, one expects an increased effect on the rotational levels of the benzene$^+$·Kr cluster cation. In fact, the spin−orbit splitting of the rotational levels is apparent at first sight in the CRIES spectra of the benzene$^+$·Kr cluster. This is demonstrated in Figure 17 showing CRIES spectra measured via the same rovibronic intermediate state of benzene$^+$·Ne (top), benzene$^+$·Ar (middle), and benzene$^+$·Kr (bottom). From the closer lying rotational levels it is obvious that the B constant is decreasing with increasing cluster mass. Furthermore, there is a small effect of the spin−orbit coupling on the rotational spectrum of benzene$^+$·Ar and a well resolved larger splitting in benzene$^+$·Kr. In particular, the CRIES spectra for intermediate states with lowest J' possible for a given value of K' clearly show two distinct J stacks separated by approximately 3 cm^{-1}. Assignment of the observed cationic rotational states leads to an accurate fit of the rotational constants of the benzene$^+$·^{84}Kr cation and the absolute energy ν_0 of the $J = 0$ level

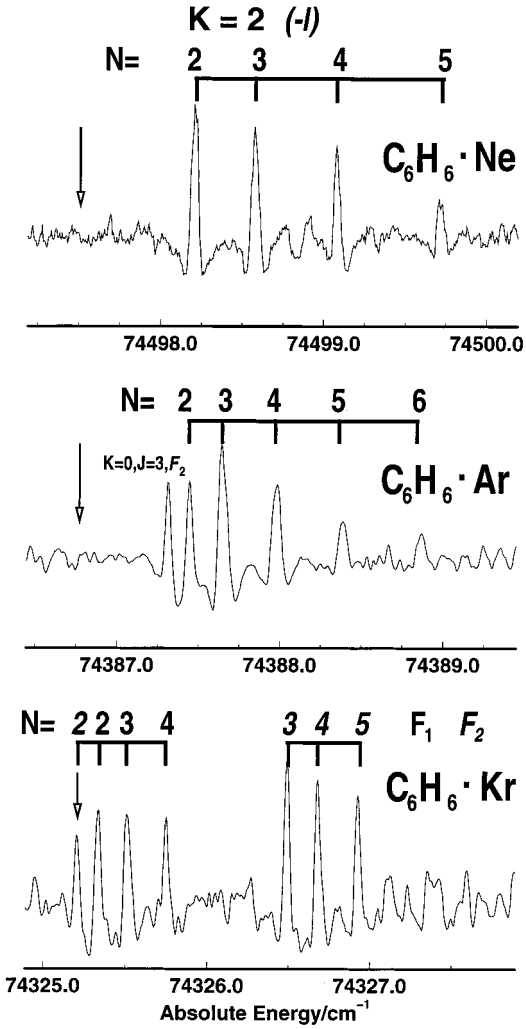

Figure 17. CRIES spectra of benzene$^+$·rare-gas clusters measured via the same selected rovibronic intermediate state S_1, 6^1, $J'_{K'} = 4_4$. Rotational spectra are plotted with the same energy scaling. Constriction of the *N*-stacks with increasing mass of the rare-gas atom demonstrates the decreasing rotational constants *B*. The arrows indicate the zero rotational levels. Note that this corresponds to the adiabatic ionization energy only in the case of benzene$^+$·Ne with no measurable effects of spin−orbit coupling. While the spin−orbit coupling is not evident from first sight in benzene$^+$·Ar, a clear splitting exists in the case of benzene$^+$·Kr. F_1 and F_2 denote the upper and lower spin−orbit component, respectively. The absolute energy scaling reflects the lowering of the benzene ionization energy upon complexation with different rare-gas atoms and is caused by the increasing binding energy of the cationic clusters.

for an assumed vanishing spin−orbit coupling constant. The values found are summarized in Table 6, and deduced values for the average van der Waals bond length and the shift of the binding energy are included in Table 7. The measured spin−orbit coupling constant of 2.94 cm^{-1} is included in Table 8.

We formally discuss the corrected rotational constants in terms of a structure of the van der Waals complex. In each case, there is a decrease in the van der Waals bond length after ionization in benzene$^+$·rare-gas clusters. This is in line with the general trend expected from a charge-induced dipole interaction in addition to the dispersion interaction stabilizing the cluster and shortening the bond length. However, the bond lengths evaluated using Kraitchman's equations are *average* bond lengths which neglect the large-amplitude zero-point van der Waals vibrations. For the case of benzene$^+$·Kr, another point has to be addressed. The experimental data was best fit to a Hund's case (*b*) (see eq 3); stronger coupling of the spin would result in an equivalent to a Hund's case (*a*) leading to a modified formula for the rotational energy levels[116] with an *effective* $B_{\text{eff}} = B(1 \pm B/a\zeta_{\text{eff}}d)$. In the intermediate regime between Hund's case (*a*) and (*b*), the values of *B* and *a* are not fully decoupled. This could lead to an error in the fitted value of *B* and thus for the evaluated van der Waals bond length in the benzene$^+$·Kr cluster. Different from the neutral excited S_1 state, the differences in the binding energy, expressed by the shift of the ionization energies of the clusters from that of the benzene monomer, no longer follow a linear dependence on the polarizability of the rare-gas atoms. This finding shows that there is an additional contribution to the dispersion interaction from a charge-induced interaction.

F. Enhanced Spin–Orbit Coupling by a Heavy Atom

A major result of the high Rydberg spectroscopy of the benzene$^+$·rare-gas cluster cations is the finding that there exists a resolved spin−orbit coupling in benzene$^+$·Ar and benzene$^+$·Kr. The measured spin−orbit coupling constant increases from Ar to Kr as a cluster partner by a factor of 6. Within the resolution of 0.02 cm^{-1} in the experiments, no measurable effects of spin−orbit coupling were found in the benzene$^+$ monomer and in the benzene$^+$·Ne cluster ion. We ascribe the origin of the effect to an enhancement of spin−orbit coupling by the attached loosely bound external heavy atom representing the onset of a microsolvation of the benzene cation with noble gases. Therefore, the investigated systems represent a microscopic example for the *external heavy atom effect* (EHA) first discovered in solution by Kasha.[118] Its origin is an enhanced spin−orbit coupling strength induced by the heavy atom in the surrounding solvent. Since then, many manifestations of the EHA have been obtained in liquid and rigid solutions,[119−121] doped molecular crystals,[122−124] and rare-gas matrices.[125,126] Most investigations have focused on the fluorescence quenching of triplet state decay or on the enhancement of $T_1 \leftarrow S_0$ absorption in neutral molecules. Gas-phase measurements of the influence of the EHA on the triplet lifetime in neutral van der Waals clusters were published for tetracene·Kr and tetracene·Xe,[127] octatetraene·rare-gas clusters,[128] 9-methoxyanthracene·rare-gas clusters,[129] and benzene·Ar and benzene·Kr,[130] whereas a lack of an EHA was reported for 9-cyanoanthracene·rare-gas clusters.[131] The EHA on benzene has been studied so far in solution and in rare-gas matrices as will be summarized below. In contrast to the *internal* heavy atom effect, the theoretical understanding of the underlying mechanisms of the EHA is still incomplete. At present, two main types of interpretations of the EHA, the exchange[132] and charge transfer[133−135] mechanisms, are being discussed.

High-resolution measurements of spin−orbit coupling are expected to shed light on the mechanism

of the underlying effect. To compare our new results on larger molecules with existing models, we discuss data currently available only for small molecule clusters. Spectroscopically resolved spin−orbit splitting has been reported for small radicals[137] and open-shell van der Waals clusters of small radicals, e.g., SH·rare gases.[138] The effects of the cluster constituents on the spin−orbit splitting were extensively studied for neutral alkaline·rare-gas clusters[139−143] and cationic alkaline earth clusters containing rare gases.[144,145] These small diatomic systems offer the possibility of an adequate theoretical treatment of the effect[146,147] in contrast to the more complex systems containing polyatomic molecules.[120] The spin−orbit splitting of Mg in a Mg·rare-gas complex was estimated to be 61.0 cm^{-1} from its atomic value without taking into account an EHA caused by the cluster partner, but larger values of 75, 140, and 260 cm^{-1} were found in Mg·rare-gas complexes containing Ar, Kr, and Xe, respectively. In addition, the splitting decreases for higher vibrational levels. Similar observations were made for neutral alkali-metal·rare-gas van der Waals complexes.[140−142] One of the presented possible explanations[139] is that spin−orbit interaction in the isolated metal atom may increase significantly if the cluster wave function has mixed in the character of the highly excited rare-gas atomic configurations. The rare-gas atom Rydberg states of the form $np^5(n + 1)s^1$ have a *p-hole* character with large spin−orbit splittings comparable to the respective values of the rare-gas ions. The spin−orbit splitting of these neutral terms are 782, 1649, and 5220 cm^{-1} for Ne, Ar, and Kr, respectively. They are expected to mix into the $Mg^+(p\pi)$·rare-gas states producing the observed larger spin−orbit splitting. For the metal-ion complexes, this mechanism seems reasonable, since the charge-induced dipole mechanism responsible for their bonding polarizes the rare-gas atoms toward the metal, removing partial electron density. As the spin−orbit splittings of the rare-gas states under discussion are very large, a small admixture was expected to be enough to explain the enhanced splittings in the clusters. However, with this mechanism the spin−orbit multiplets are expected to be inverted. Another plausible mechanism involves a charge transfer state of the cluster. If the electron in the excited p orbital of Mg^+ is diffuse enough, it may have some density in the region of the rare-gas atom. The increased spin−orbit interaction would then arise from small admixtures of the configuration Mg^{2+}·$(\text{rare gas})^-$. This mechanism would result in a normal spin−orbit multiplet order. Although rotational resolution was achieved in a study of Mg^+·Ar, the lowest rotational transitions could not be clearly resolved, thus preventing a determination of the multiplet order present in the spectra.[145] Recent theoretical work at SCF and CI ab initio levels[147] propose the mixing of rare-gas ($np\pi$) character into the $Mg^+(3p\pi)$ MO, implying little charge transfer. This finding supports the first mechanism discussed above and is strengthened by an earlier work on Li·Ar and Li·Ne.[146] In both cases, the enhancement of spin−orbit coupling depends strongly on interatomic distances[147] in the diatomic systems.

The situation is clearly more complicated in polyatomic systems and to date beyond the feasibility of accurate ab initio calculations. In a very recent work, the restrictions of a pseudodiatomic approximation when treating spin−orbit splitting in small polyatomic systems such as I·CO_2 or I·OCS were pointed out.[148] For the case of the benzene cation investigated here, no experimental or theoretical data is available to compare with our results. In recent high-resolution experiments on the larger polyatomic benzene cation[88] and on hexafluorobenzene,[87] no evidence for effects of spin−orbit coupling on the rotational energy levels was found. However, several groups investigated the phosphorescence decay of neutral benzene in rare-gas matrices.[125,136,149−152] In these studies, no deuterium effect on the triplet lifetimes in rare-gas matrices was observed,[125] a finding which we also report for the spin−orbit coupling constant of the $benzene^+$ cation in its ground state in van der Waals clusters with a single perturbing heavy atom. The theoretical work of Lin and Lin on the influence of the mere electrostatic interaction of the perturbed benzene orbitals and the nucleus of the perturbing rare-gas atoms[153] gave values which are comparable to the internal spin−orbit matrix elements of benzene.[154] These are far too small to explain the observed decay rate of the triplet state of benzene in a rare-gas matrix.[151,152] Further, in a more qualitative interpretation of Lin's results based on electrostatic interaction, a rare-gas atom located right above or below the benzene ring in the rare-gas matrix does not contribute to the external spin−orbit matrix element. The same applies to the rare-gas atoms located in the benzene plane. This was explained by the extension of the π-orbitals of benzene perpendicular to the benzene plane and the negligible extension of the rare-gas nuclei. Therefore, the theory of Lin and Lin[153] does not account for the spin−orbit enhancement by the heavy atom in benzene·rare-gas van der Waals clusters observed in this work. It is more likely that the other two discussed mechanisms (exchange or charge transfer) are responsible for the observed effect on spin−orbit coupling. An argument against an effective charge-transfer process being responsible for the enhanced spin−orbit coupling is the high ionization energy of the rare-gas atoms in the cluster (Ar 15.7 eV, Kr 14.0 eV). As a result, we ascribe the observed spin−orbit coupling to an exchange mechanism. Detailed theoretical investigations now appear to be possible for this clear experimental situation with the heavy atom in a distinct position and precisely determined spin−orbit matrix elements. In the case of $benzene^+$·Ar and $benzene^+$·Kr, the spin−orbit doublets are in the normal order,[111] i.e., the F_1 spin−orbit components are lower in energy than the respective F_2 components.

G. Rydberg Series above the Lowest Ionization Energy: van der Waals Modes of Ionic Clusters

Our investigations of Rydberg states were extended to the region several tens of cm^{-1} above the lowest ionization threshold of benzene·rare-gas van der Waals clusters. To avoid the high background of prompt ions produced in a direct ionization process,

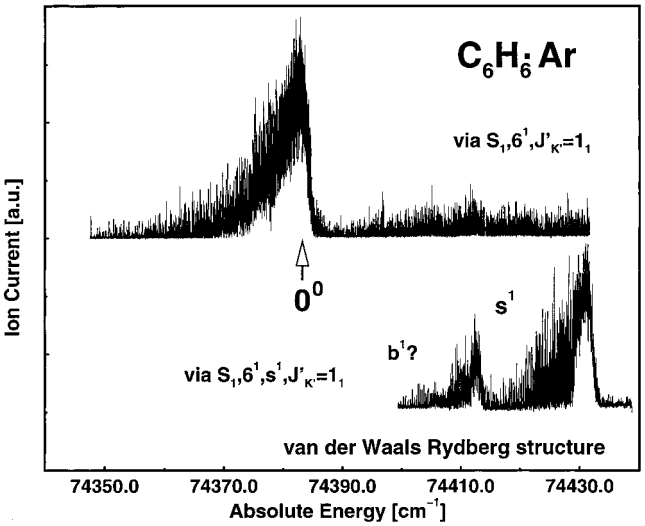

Figure 18. Upper trace: Rydberg spectrum of benzene·Ar cluster below and above the lowest ionization energy (0^0) measured via the S_1, 6^1, $J'_{K'} = 1_1$ intermediate state with no van der Waals vibration excited. Prompt ions and molecules ionized in Rydberg states above $n \approx 200$ are removed by a weak electric prepulse with 100 ns delay after the laser pulse. Note that there is signal above the lowest ionization energy showing resolvable Rydberg structure. Lower trace: Rydberg spectrum excited via the same rotational intermediate state $J'_{K'}$ but with 1 quantum of the van der Waals stretching mode excited in addition to the benzene skeletal mode 6^1. Note the clear Rydberg structure above the lowest ionization threshold. For explanation, see text.

a modified detection scheme was used. While the laser excitation takes place under field-free conditions, an additional field pulse of 0.7 V/cm and 45 μs duration is applied to separate the prompt ions from the neutral Rydberg clusters as described in section III.B. Figure 18 shows a Rydberg spectrum of the C_6H_6·Ar van der Waals cluster (upper trace) measured via the S_1, 6^1 intermediate state. Besides the surprising result that even low Rydberg states ($n \approx 50$) survive the long delay time of 45 μs, the spectrum shows another interesting detail. There is Rydberg structure above the lowest ionization threshold of the cluster. It originates from Rydberg series converging to low-frequency vibrational states representing slow relative motions of the cluster components of the cationic core. It is known from MATI experiments that the intensity of transitions into states with excited van der Waals vibrations is enhanced when an intermediate state with the same van der Waals vibration is excited because of the better Franck−Condon factors.[113] Taking spectra via 1 quantum of the van der Waals stretching mode excited in the S_1 intermediate state allows us to obtain Rydberg spectra converging to the stretching mode in the cluster ion. The result is shown in the lower trace of Figure 18. The spectrum consists of two energetic regions with series converging to limits around 30 and 48 cm^{-1} above the lowest ionization energy. (The series limits of the strongest Rydberg series are 74 416.953 and 74 435.653 cm^{-1}, respectively.) In both cases a pronounced resolved Rydberg structure with an excellent signal-to-noise ratio is observed. The series limits of the single Rydberg series in the dense Rydberg spectrum can be evaluated using the cross correlation technique described in section III.D. A closer analysis reveals that the rotational level structure of the higher van der Waals vibrational mode (48 cm^{-1}) is very similar to that of the vibrationless ionic ground state while the lower lying van der Waals mode (30 cm^{-1}) has a completely different rotational structure. This suggests that the higher van der Waals mode is a stretching mode with the same symmetry as the vibrationless ground state while the lower van der Waals mode has a different symmetry and is most likely the first quantum of the bending vibration. The distinction of van der Waals modes with different symmetry by their different rotational structure in the cationic ground state will be very useful for the assignment of the van der Waals level structure of benzene$^+$·Ar and other clusters in their neutral S_1 and cationic ground states.[3,113,155]

To date, no spectra of van der Waals modes of the benzene·Ne cluster have been reported, neither for the neutral S_0 and S_1 states of the cluster nor for the ionic cluster molecule. Here, the interesting question is how many vibrational states exist in the intermolecular potential with small dissociation energy. From high-resolution REMPI experiments of the $S_1 \leftarrow S_0$ transition in benzene·Ne, the existence of large-amplitude van der Waals vibrations was demonstrated by the large isotopic shift of the average van der Waals bond length of 6 mÅ between C_6H_6·^{20}Ne and C_6H_6·^{22}Ne.[55] However, a direct observation of excited van der Waals modes was not possible. As the van der Waals binding strength increases by 56.76 cm^{-1} from the excited neutral S_1 state of the cluster to the catonic ground state (see section III.E.1), the intermolecular vibrations seem to be spectroscopically accessible in the cluster cation. In fact, scanning the region a couple of cm^{-1} above the lowest ionization energy in our high-resolution double-resonance experiment, Rydberg signal is found in this range. The structure is too dense to resolve single Rydberg states. However, there is evidence of Rydberg series converging to an intermolecular van der Waals vibrational state between 7 and 13 cm^{-1} above the lowest ionization treshold and another to higher lying modes of more than 13 cm^{-1}. Our study of this interesting system is continuing.

IV. Summary and Conclusions

In this work we report on recent applications of mass-resolved high-resolution UV spectroscopy techniques. During the past years their application has been extended from aromatic-molecule·noble-gas clusters to hydrogen-bonded aromatic·water systems and from neutral clusters to ionized ones. For the analysis of the highly resolved rotational structure of vibronic bands of these complexes, computer-assisted cross correlation techniques are becoming more and more important. They allow the determination of the values of rotational constants by pattern recognition methods without detailed assignments of the rotational lines, which is particularly complicated in asymmetric clusters. We demonstrate the possibilities of the new methods for three aromatic-molecule·water clusters which are typical for this class of clusters and show different kinds of bonding between the aromatic molecule and the water attached to it.

In benzonitrile with its strong dipole moment, the water is found to be in a nested position between the CN group and the *ortho*-hydrogen with two principal ponts of attraction differing in their van der Waals and hydrogen-bonding character. As a second example, the indole molecule is chosen which is the chromophore of the amino acid tryptophan. Here, the indole molecule acts as a proton donor with a linear hydrogen bond between the amino-hydrogen and the water molecule. We support the experimentally found structures by fully optimized ab initio geometry calculations on the HF level. In the phenol·water cluster, we study the intermolecular vibrational dynamics in the hydrogen-bonding potential between the OH group and the water molecule. In particular, the tunnel splitting of the various intermolecular vibronic bands is investigated by autocorrelation techniques and by an analysis of the individual rotational constants of the various bands. This leads to an assignment of the second overtone of the torsional motion of the water which is of basic importance for the understanding of the hydrogen-bonding potential between the OH group and the water molecule.

In a second part of this article, we review a new approach to rotationally resolved spectroscopy of ionic clusters. These techniques are based on the excitation and resolution of high Rydberg states in the range $40 \lesssim n \lesssim 110$ of the neutral molecule or cluster under field-free conditions in a high-resolution double-resonance excitation experiment. The extrapolation of the resolved high Rydberg states leads to accurate series limits representing the rotational states of the cluster cation. Choosing different intermediate states in the double-resonance excitation results in the identification of a large number of different rotational states of the cluster cation, on which a rotational analysis can be performed. We demonstrate the possibilities of this new technique for the prototype benzene·noble-gas dimers and obtain the structure of the cationic clusters with the average van der Waals distance of the noble-gas atom from the benzene cation. For the heavy noble gases Ar and Kr, a spin−orbit splitting of the rotational levels of the cluster is observed providing a precise spectroscopic manifestation of the external heavy atom effect with the perturber in a defined, well-known position from the perturbed system.

Future work will include the extension of these new techniques to larger systems and various kinds of hydrogen bonds. In particular, changes in the geometry after ionization and for different chemical surroundings are of interest as different charge distributions are expected to influence the strength and geometry of the hydrogen bonding. Combining the new experimental techniques described in this work with theoretical approaches will help to clarify this problem which is of basic interest to explain sovation processes in chemistry and the stability of biomolecules in their natural surroundings.

V. Acknowledgment

The authors thank R. Neuhauser and R. M. Helm for valuable discussions and Th. Mehnert for performing the calculations. Financial support from the Deutsche Forschungsgemeinschaft and the Fonds der Chemischen Industrie is gratefully acknowledged.

VI. References

(1) For a review, see: Entire issue van der Waals Molecules II. *Chem. Rev.* **1994**, *94*.
(2) Lin, S. H.; Fujimura, Y.; Neusser, H. J.; Schlag, E. W. *Multiphoton Spectroscopy of Molecules, Quantum Electronics, Principles and Applications*; Academic Press: New York, 1984.
(3) Neusser, H. J.; Sussmann, R.; Smith, A. M.; Riedle, E.; Weber, Th. *Ber. Bunsen-Ges. Phys. Chem.* **1992**, *96*, 1252.
(4) Neusser, H. J.; Krause, H. *Chem. Rev.* **1994**, *94*, 1829.
(5) Gerstenkorn, S.; Luc, P. *Atlas du spectre d'absorption de la molecule d'Iode*; Centre du National de la Recherche Scientifique, CNRS: Paris, 1978.
(6) Baskin, J. S.; Felker, P. M.; Zewail, A. H. *J. Chem. Phys.* **1986**, *84*, 4708.
(7) Felker, P. M. *J. Phys. Chem.* **1992**, *96*, 7844.
(8) Joireman, P. W.; Ohline, Sh. M.; Felker, P. M. *J. Phys. Chem. A* **1998**, *102*, 4481.
(9) Andrews, P. M.; Pryor, B. A.; Berger, M. B.; Palmer, P. M.; Topp, M. R. *J. Phys. Chem. A* **1997**, *101*, 6222.
(10) Fujiwara, T.; Fujimura, Y.; Kajimoto, O. *Chem. Phys. Lett.* **1996**, *261*, 201.
(11) Riehn, Ch.; Weichert, A.; Zimmermann, M.; Brutschy, B. *Chem. Phys. Lett.* **1999**, *299*, 103.
(12) Troxler, T.; Smith, P. G.; Stratton, J. R.; Topp, M. R. *J. Chem. Phys.* **1994**, *100*, 797.
(13) Magnera, Th. F.; Sammond, D. M.; Michl, J. *Chem. Phys. Lett.* **1993**, *211*, 378.
(14) Helm, R. M.; Neusser, H. J. *Chem. Phys.* **1998**, *239*, 33.
(15) Haynam, C. A.; Brumbaugh, D. V.; Levy, D. H. *J. Chem. Phys.* **1984**, *81*, 2282. Wu, Y. R.; Levy, D. H. *J. Chem. Phys.* **1989**, *91*, 5278.
(16) Philips, L. A.; Levy, D. H. *J. Chem. Phys.* **1986**, *85*, 1327.
(17) Weber, Th.; von Bargen, A.; Riedle, E.; Neusser, H. J. *J. Chem. Phys.* **1990**, *92*, 90.
(18) Berden, G.; Meerts, W. L.; Schmitt, M.; Kleinermanns, K. *J. Chem. Phys.* **1996**, *104*, 972.
(19) Berden, G.; Meerts, W. L.; Plusquellic, D. F.; Fujita, I.; Pratt, D. W. *J. Chem. Phys.* **1996**, *104*, 3935.
(20) Helm, R. M.; Vogel, H.-P.; Neusser, H. J. *Chem. Phys. Lett.* **1997**, *270*, 285.
(21) Press: W. H.; Teukolsky, S. A.; Vetterling, W. T.; Flannery, B. P. *Numerical recipes in C: The art of scientific computing*; Cambridge University Press: Cambridge, 1992.
(22) Weber, Th.; Neusser, H. J. *J. Chem. Phys.* **1991**, *94*, 7689.
(23) Korter, T. M.; Küpper, J.; Pratt, D. W. *J. Chem. Phys.* **1999**, *111*, 3946.
(24) Rettig, W. *Angew. Chem., Int. Ed. Engl.* **1986**, *25*, 971.
(25) Grabowski, Z. R.; Rotkiewicz, K.; Siemiarczuk, A.; Cowley, D. J.; Baumann, W. *Nuov. J. Chim.* **1979**, *3*, 443.
(26) Weast, R. C.; Astle, M. J. *Handbook of chemistry and physics*; CRC Press: Boca Raton, 1979.
(27) Held, A.; Pratt, D. W. *J. Am. Chem. Soc.* **1993**, *115*, 9708.
(28) Helm, R. M.; Clara, M.; Grebner, Th. L.; Neusser, H. J. *J. Phys. Chem. A* **1998**, *102*, 3268.
(29) Braun, J. E.; Grebner, Th. L.; Neusser, H. J. *J. Phys. Chem.* **1998**, *102*, 3273.
(30) Korter, T. M.; Pratt, D. W.; Küpper, J. *J. Phys. Chem. A* **1998**, *102*, 7211.
(31) Helm, R. M.; Vogel, H.-P.; Neusser, H. J.; Storm, V.; Consalvo, D.; Dreizler, H. *Z. Naturforsch.* **1997**, *52a*, 655.
(32) Dahmen, U.; Stahl, W.; Dreizler, H. *Ber. Bunsen-Ges. Phys. Chem.* **1994**, *98*, 970.
(33) Dahmen, U. Diploma Thesis; Universität Kiel, 1993.
(34) Lucia, F. C.; Helminger, P.; Gordy, W. *Phys. Rev. A* **1973**, *8*, 2785.
(35) Melandri, S.; Consalvo, D.; Caminati, W.; Favero, P. G. *J. Chem. Phys.* **1999**, *111*, 3874.
(36) Mehnert, Th. Diploma Thesis; Technische Universität München, 2000.
(37) Kobayashi, K.; Kajimoto, O. *J. Chem. Phys.* **1987**, *86*, 1118.
(38) Mordzinski, A.; Sobolewski, A. L.; Levy, D. H. *J. Phys. Chem. A* **1997**, *101*, 8221.
(39) Sakota, K.; Nishi, K.; Ohashi, K.; Sekiya, H. *Chem. Phys. Lett.* **2000**, *322*, 407.
(40) Sobolewski, A. L.; Domcke, W. *Chem. Phys. Lett.* **1996**, *250*, 428. Sobolewski, A. L.; Domcke, W. *Chem. Phys. Lett.* **1996**, *259*, 119.
(41) Huang, K.-T.; Lombardi, J. R. *J. Chem. Phys.* **1971**, *55*, 4072.
(42) Tubergen, M. J.; Levy, D. H. *J. Phys. Chem.* **1991**, *95*, 2175.
(43) Hager, J.; Ivanco, M.; Smith, M. A.; Wallace, S. C. *Chem. Phys.* **1986**, *105*, 397. Hager, J.; Ivanco, M.; Smith, M. A.; Wallace, S. C. *Chem. Phys. Lett.* **1985**, *113*, 503.
(44) Caminati, W.; di Bernando, S. *J. Mol. Struct.* **1990**, *240*, 253.
(45) Outhouse, E. A.; Bickel, G. A.; Demmer, D. R.; Wallace, S. C. *J. Chem. Phys.* **1991**, *95*, 6261.

(46) Lipert, R. J.; Bermudez, G.; Colson, S. D. *J. Phys. Chem.* **1988**, *92*, 3801.
(47) Barstis, T. L. O.; Grace, L. I.; Dunn, T. M.; Lubman, D. M. *J. Phys. Chem.* **1993**, *97*, 5820.
(48) Berden, G.; Meerts, W. L.; Jalviste, E. *J. Chem. Phys.* **1995**, *103*, 9596.
(49) Remmers, K.; Jalviste, E.; Mistrik, I.; Berden, G.; Meerts, W. L. *J. Chem. Phys.* **1998**, *108*, 8436.
(50) Sammeth, D. M.; Yan, Sh.; Spangler, L. H.; Callis, P. R. *J. Phys. Chem.* **1990**, *94*, 7340.
(51) Muino, P. L.; Callis, P. R. *Chem. Phys. Lett.* **1994**, *222*, 156.
(52) Pribble, R. N.; Zwier, T. S. *Faraday Discuss.* **1994**, *97*.
(53) Suzuki, S.; Green, P. G.; Bumgarner, R. E.; Dasgupta, S.; Goddard, W. A., III; Blake, G. A. *Science* **1992**, *257*, 942.
(54) Gutowsky, H. S.; Emilsson, T.; Arunan, E. *J. Chem. Phys.* **1993**, *99*, 4883.
(55) Weber, Th.; Riedle, E.; Neusser, H. J.; Schlag, E. W. *J. Mol. Struct.* **1991**, *249*, 69.
(56) Weber, Th.; Riedle, E.; Neusser, H. J. *Z. Phys. D* **1991**, *20*, 43.
(57) Weber, Th.; Riedle, E.; Neusser, H. J.; Schlag, E. W. *Chem. Phys. Lett.* **1991**, *183*, 77.
(58) Slater, L. S.; Callis, P. R. *J. Phys. Chem.* **1995**, *99*, 8572.
(59) Jensen, F. *Introduction to Computational Chemistry*; Wiley: New York, 1999; p 264.
(60) Helm, R. M.; Vogel, H.-P.; Neusser, H. J. *J. Chem. Phys.* **1998**, *108*, 4496.
(61) Gerhards, M.; Schmitt, M.; Kleinermanns, K.; Stahl, W. *J. Chem. Phys.* **1996**, *104*, 967.
(62) Stanley, R. J.; Castleman, A. W. *J. Chem. Phys.* **1991**, *94*, 7744.
(63) Tanabe, S.; Ebata, T.; Fujii, M.; Mikami, N. *Chem. Phys. Lett.* **1993**, *215*, 347.
(64) Stanley, R. J.; Castleman, A. W., Jr. *J. Chem. Phys.* **1993**, *98*, 796.
(65) Ebata, T.; Furukawa, M.; Suzuki, T.; Ito, M. *J. Opt. Soc. Am. B* **1990**, *7*, 1890.
(66) Hartland, G.; Henson, B.; Venturo, V.; Felker, P. M. *J. Phys. Chem.* **1992**, *96*, 1164.
(67) Schütz, M.; Bürgi, T.; Leutwyler, S. *J. Chem. Phys.* **1993**, *98*, 3763.
(68) Oikawa, A.; Abe, H.; Mikami, N.; Ito, M. *J. Phys. Chem.* **1983**, *87*, 5083.
(69) Abe, H.; Mikami, N.; Ito, M. *J. Phys. Chem.* **1982**, *86*, 1768.
(70) Fuke, K.; Kaya, K. *Chem. Phys. Lett.* **1983**, *94*, 97.
(71) Lipert, R. J.; Colson, S. D. *J. Chem. Phys.* **1988**, *89*, 4579.
(72) Lipert, R. J.; Colson, S. D. *Chem. Phys. Lett.* **1989**, *161*, 303.
(73) Lipert, R. J.; Colson, S. D. *J. Phys. Chem.* **1990**, *94*, 2358.
(74) Lipert, R. J.; Colson, S. D. *J. Phys. Chem.* **1989**, *93*, 135.
(75) Dopfer, O. Doctoral Thesis; Technische Universität München, 1994.
(76) Reiser, G.; Dopfer, O.; Lindner, R.; Henri, G.; Müller-Dethlefs, K.; Schlag, E. W.; Colson, S. D. *Chem. Phys. Lett.* **1991**, *181*, 1.
(77) Dopfer, O.; Reiser, G.; Müller-Dethlefs, K.; Schlag, E. W.; Colson, S. D. *J. Chem. Phys.* **1994**, *101*, 974.
(78) Dopfer, O.; Müller-Dethlefs, K. *J. Chem. Phys.* **1994**, *101*, 8508.
(79) Schütz, M.; Bürgi, T.; Leutwyler, S. *J. Mol. Struct.* **1992**, *276*, 117.
(80) Watanabe, H.; Iwata, S. *J. Chem. Phys.* **1996**, *105*, 420.
(81) Hobza, P.; Burcl, R.; Spirko, V.; Dopfer, O.; Müller-Dethlefs, K.; Schlag, E. W. *J. Chem. Phys.* **1994**, *101*, 990.
(82) Schmitt, M.; Jacoby, Ch.; Kleinermanns, K. *J. Chem. Phys.* **1998**, *108*, 4486.
(83) Schmitt, M.; Jacoby, C.; Kleinermanns, K. *J. Chem. Phys.* **1998**, *108*, 4486.
(84) Hollas, J. M. *Symmetry in molecules*; Clowes: London, 1972.
(85) *Ion and cluster ion spectroscopy and structure*; Maier, J. P., Ed.; Elsevier: Amsterdam, 1989.
(86) *Molecular Ions: Spectroscopy, Structure and Chemistry*; Miller, T. A., Bondybey, V. E., Eds.; North-Holland: Amsterdam, 1983.
(87) Yu, L.; Foster, S. C.; Williamson, J. M.; Miller, T. A. *J. Chem. Phys.* **1990**, *92*, 5794.
(88) Neuhauser, R. G.; Siglow, K.; Neusser, H. J. *J. Chem. Phys.* **1997**, *106*, 896.
(89) Chewter, L. A.; Sander, M.; Müller-Dethlefs, K.; Schlag, E. W. *J. Chem. Phys.* **1987**, *86*, 4737.
(90) Fischer, I.; Lindner, R.; Müller-Dethlefs, K. *J. Chem. Soc, Faraday Trans.* **1994**, *17*, 2425.
(91) Zhu, L.; Johnson, P. M. *J. Chem. Phys.* **1991**, *94*, 5769.
(92) Krause, H.; Neusser, H. J. *J. Chem. Phys.* **1992**, *97*, 5923.
(93) Siglow, K.; Neuhauser, R.; Neusser, H. J. *J. Chem. Phys.* **1999**, *110*, 5589.
(94) Duncan, A. B. F. *Rydberg Series in Atoms and Molecules*; Academic Press: New York, 1971.
(95) Gallagher, Th. F. *Rydberg Atoms*; Cambridge Monographs: Cambridge, 1994.
(96) Neuhauser, R.; Neusser, H. J. *Chem. Phys. Lett.* **1996**, *253*, 151.
(97) Neuhauser, R.; Siglow, K.; Neusser, H. J. *Phys. Rev. Lett.* **1998**, *80*, 5089.
(98) Bixon, M.; Jortner, J. *J. Phys. Chem.* **1995**, *99*, 7466.
(99) Bordas, C.; Brevet, P. F.; Broyer, M.; Chevaleyre, J.; Labastie, P.; Petto, J. P. *Phys. Rev. Lett.* **1988**, *60*, 917.
(100) Chupka, W. A. *J. Chem. Phys.* **1993**, *98*, 4520.
(101) Chupka, W. A. *J. Chem. Phys.* **1993**, *99*, 5800.
(102) Merkt, F.; Zare, R. N. *J. Chem. Phys.* **1994**, *101*, 3495.
(103) Jortner, J.; Bixon, M. *J. Chem. Phys.* **1995**, *102*, 5636.
(104) Jortner, J.; Bixon, M. *Ber. Bunsen-Ges. Phys. Chem.* **1995**, *99*, 296.
(105) Siglow, K.; Neusser, H. J. *J. Chem. Phys.* **2000**, *112*, 647.
(106) Remacle, F.; Levine, R. D. *J. Chem. Phys.* **1996**, *105*, 4649.
(107) Baranov, L. Y.; Remacle, R.; Levine, R. D. *Phys. Rev A* **1996**, *54*, 4789.
(108) Neuhauser, R.; Neusser, H. J. *Comm. At. Mol. Phys.*, in press.
(109) Siglow, K.; Neuhauser, R.; Neusser, H. J. *Chem. Phys. Lett.* **1998**, *293*, 19.
(110) See http://ruppert.phys.chemie.tu-muenchen.de/clusterdata.html.
(111) Herzberg, G. *Molecular spectra and molecular structure*; Van Nostrand: Princeton, 1967; Vol. III, Chapter I.
(112) Kraitchman, J. *Am. J. Phys.* **1953**, *21*, 17.
(113) Krause, H.; Neusser, H. J. *Chem. Phys. Lett.* **1993**, *213*, 603.
(114) Lindner, R.; Müller-Dethlefs, K.; Wedum, E.; Haber, K.; Grant, E. R. *Science* **1996**, *271*, 1698.
(115) Krause, H.; Neusser, H. J. *J. Chem. Phys.* **1993**, *99*, 6278.
(116) Brown, J. M. *Mol. Phys.* **1971**, *20*, 817.
(117) van Vleck, J. H. *Rev. Mod. Phys.* **1951**, *23*, 213.
(118) Kasha, M. *J. Chem. Phys.* **1952**, *20*, 71.
(119) McGlynn, S. P.; Azumi, T.; Kasha, M. *J. Chem. Phys.* **1964**, *40*, 507.
(120) McGlynn, S. P.; Azumi, T.; Kinoshita, M. *Molecular spectroscopy of the triplet state*; Prentice Hall: Englewood Cliffs, 1969; p 307.
(121) Klimchuk, E. S.; Makarov, B. P.; Serebrennikov, Qu. A.; Khudyakov, I. V. *Bull. Acad. Sci. USSR Chem. Sci.* **1989**, *38*, 1627.
(122) Weinzierl, G.; Friedrich, J. *Chem. Phys. Lett.* **1981**, *80*, 55.
(123) Komada, Y.; Yamaushi, S.; Kirota, N. *J. Chem. Phys.* **1985**, *82*, 1651.
(124) Yamaguchi, S.; Saigusa, H.; Azumi, T. *J. Chem. Phys.* **1981**, *74*, 5335.
(125) Hsu, Y. P.; Johnson, P. M. *J. Chem. Phys.* **1973**, *59*, 136.
(126) Morgan, M. A.; Pimentel, G. C. *J. Phys. Chem.* **1989**, *93*, 3056.
(127) Amirav, A.; Even, U.; Jortner, J. *Chem. Phys. Lett.* **1979**, *67*, 9.
(128) Kim, T.-S.; Choi, Y. S.; Yoshihara, K. *Chem. Phys. Lett.* **1995**, *247*, 541.
(129) Hirayama, S.; Tanaka, F.; Shobatake, K. *Chem. Phys. Lett.* **1988**, *153*, 112.
(130) Neusser, H. J.; Neuhauser, R. *Adv. Chem. Phys.* **1997**, *101*, 409.
(131) Hirayama, S.; Shobatake, K.; Tabayashi, K. *Chem. Phys. Lett.* **1985**, *121*, 228.
(132) Hoijtink, G. J. *Mol. Phys.* **1960**, *3*, 67.
(133) Minaev, B. F.; Knuts, S.; Agren, H. *Chem. Phys.* **1994**, *181*, 15.
(134) Tsubomura, H.; Mulliken, R. S. *J. Am. Chem. Soc.* **1960**, *82*, 5966.
(135) Murrell, J. N. *Mol. Phys.* **1960**, *3*, 319.
(136) Robinson, G. W. *J. Mol. Spectrosc.* **1961**, *6*, 58.
(137) Cerny, T. M.; Tan, X.-Q.; Williamson, J. M.; Robles, E. S. J.; Ellis, A. M.; Miller, T. A. *J. Chem. Phys.* **1993**, *99*, 9376. Tan, X.-Q.; Yang, M.-C.; Carter, C. C.; Williamson, J. M.; Miller, T. A.; Mlsna, T. E.; Anderson, J. D. O.; Desmarteau, D. D. *J. Phys. Chem.* **1994**, *98*, 2732. Cerny, T. M.; Williamson, J. M.; Miller, T. A. *J. Chem. Phys.* **1995**, *102*, 2372.
(138) Carter, C. C.; Miller, T. A. *J. Phys. Chem.* **1997**, *107*, 3447.
(139) Breckenridge, W. H. et al. In *Advances in metal and semiconductor clusters*; Duncan, M. A., Ed.; JAI: Greenwich, 1995; Vol. III.
(140) Smalley, R. E.; Auerbach, D. A.; Fitch, P. S. H.; Levy, D. H.; Wharton, L. *J. Chem. Phys.* **1977**, *66*, 3778.
(141) Cooper, D. L. *J. Chem. Phys.* **1981**, *75*, 4157.
(142) Brühl, R.; Kapetanakis, J.; Zimmermann, D. *J. Chem. Phys.* **1991**, *94*, 5865.
(143) Partridge, H.; Bauschlicher, Ch. W.; Langhoff, S. R. *J. Phys. Chem.* **1992**, *96*, 5350.
(144) Pilgrim, J. S.; Yeh, C. S.; Berry, K. R.; Duncan, M. A. *J. Chem. Phys.* **1994**, *100*, 7945. Scurlock, C. T.; Pilgrim, J. S.; Duncan, M. A. *J. Chem. Phys.* **1996**, *105*, 7876. Reddic, J. E.; Duncan, M. A. *J. Chem. Phys.* **1999**, *110*, 9948.
(145) Scurlock, C. T.; Pilgrim, J. S.; Duncan, M. A. *J. Chem. Phys.* **1995**, *103*, 3293.
(146) Sohlberg, K.; Yarkony, D. R. *J. Chem. Phys.* **1997**, *107*, 7690.
(147) Matsika, S.; Pitzer, R. M. *J. Phys. Chem. A* **1998**, *102*, 1652.
(148) Sanov, A.; Faeder, J.; Parson, R.; Lineberger, W. C. *Chem. Phys. Lett.* **1999**, *313*, 812.
(149) Robinson, G. W.; Frosch, R. P. *J. Chem. Phys.* **1963**, *38*, 1187.
(150) Johnson, P. M.; Ziegler, L. *J. Chem. Phys.* **1972**, *56*, 2169.
(151) Giachino, G. G.; Kearns, D. R. *J. Chem. Phys.* **1970**, *52*, 2964.
(152) Hofeldt, R. H.; Sahai, R.; Lin, S. H. *J. Chem. Phys.* **1970**, *53*, 4512.
(153) Lin, K. C.; Lin, S. H. *Mol. Phys.* **1971**, *21*, 1105.
(154) Xu, Y. J.; McKellar, A. R. W. *J. Mol. Spectrosc.* **1997**, *184*, 202.
(155) Menapace, J. A.; Bernstein, E. R. *J. Phys. Chem.* **1987**, *91*, 2533.

CR9900578